Functional and spatial proteomics profiling reveals intra- and intercellular signaling crosstalk in colorectal cancer

Christina Plattner[1,13], Giorgia Lamberti[1,13], Peter Blattmann[2,13,14], Alexander Kirchmair[1,13], Dietmar Rieder[1], Zuzana Loncova[1], Gregor Sturm[1], Stefan Scheidl[3], Marieke Ijsselsteijn[4], Georgios Fotakis[1], Asma Noureen[1], Rebecca Lisandrelli[1], Nina Böck[1], Niloofar Nemati[1], Anne Krogsdam[1], Sophia Daum[1,15], Francesca Finotello[1,16], Antonios Somarakis[5], Alexander Schäfer[2], Doris Wilflingseder[6], Miguel Gonzalez Acera[7], Dietmar Öfner[3], Lukas A. Huber[8], Hans Clevers[9], Christoph Becker[7], Henner F. Farin[10,11,12], Florian R. Greten[10,11,12], Ruedi Abersold[2], Noel Filipe da Cunha Carvalho de Miranda[4], Zlatko Trajanoski[1]*

[1]Biocenter, Institute of Bioinformatics, Medical University of Innsbruck, Austria
[2]Department of Biology, Institute of Molecular Systems Biology, ETH Zurich, Switzerland
[3]Department of Visceral, Transplant and Thoracic Surgery, Medical University of Innsbruck, Austria
[4]Department of Pathology, Leiden University Medical Center, Leiden, The Netherlands
[5]Department of Radiology, Leiden University Medical Center, Leiden, The Netherlands
[6]Institute of Hygiene and Medical Microbiology, Medical University of Innsbruck, Austria
[7]Department of Medicine 1, University of Erlangen-Nuremberg, Erlangen, Germany
[8]Biocenter, Institute of Cell Biology, Medical University of Innsbruck, Austria
[9]Hubrecht Institute, Utrecht, The Netherlands
[10]Institute for Tumor Biology and Experimental Therapy, Georg-Speyer-Haus Frankfurt/Main, Germany
[11]Frankfurt Cancer Institute, Goethe University, Frankfurt am Main, Germany
[12]German Cancer Consortium (DKTK), Heidelberg, Germany
[13]These authors contributed equally to this work
[14]Current address: Idorsia Pharmaceuticals Ltd, Allschwil, Switzerland
[15]Current address: Department of Internal Medicine V (Hematology and Oncology), Medical University of Innsbruck, Austria
[16]Current address: Institute of Molecular Biology & Digital Science Center (DiSC), University of Innsbruck, Austria

*Correspondence: Zlatko Trajanoski, PhD
Biocenter, Institute of Bioinformatics, Medical University of Innsbruck,
Innrain 80, 6020 Innsbruck, Austria
Email: zlatko.trajanoski@i-med.ac.at

Abstract

Background: Despite major advances in the development of targeted therapies, precision (immuno)oncology approaches for patients with colorectal cancer continue to lag behind other solid cancers. Functional precision oncology – a strategy that is based on perturbing primary tumor cells from cancer patients with drugs – could provide an alternate road forward to personalize treatment.

Methods: We extend here the functional precision oncology paradigm to measuring phosphoproteome landscapes using patient-derived organoids (PDOs). We first employed steady-state multi-omics (exome sequencing, RNA sequencing, and proteomics) and single-cell characterization of the PDOs. The PDOs were then perturbed with kinase inhibitors (MEKi, PI3Ki, mTORi, TBKi, BRAFi, and TAKi), and large-scale phosphoproteomics profiling using data-independent acquisition was carried out. Further, we used imaging mass-cytometry-based single-cell proteomic profiling of the primary tumors to characterize cellular composition of the tumor-microenvironment (TME) and to quantify heterocellular signaling crosstalk.

Results: We show that kinase inhibitors induce profound off-target effects resulting in a crosstalk with oncogenic and immune-related pathways. Reconstruction of the topologies of the kinase networks revealed that the patient-specific rewiring of the central EGFR-RAS-MAPK network is unaffected by mutations. Moreover, we show non-genetic heterogeneity of the PDOs and patient- and inhibitor-specific upregulation of stemness and differentiation genes by kinase inhibitors. We complemented our functional profiling by spatial proteomics profiling of the primary tumors using imaging mass cytometry. We quantify spatial heterocellular crosstalk and tumor-immune cell interactions, showing an avoidance of PD1+ immune cells and PD-L1+ tumor cells.

Conclusions: Collectively, we provide a multi-modal framework for inferring tumor cell intrinsic signaling and external signaling from the TME to inform precision (immuno)-oncology in colorectal cancer.

Keywords

Kinase networks, functional precision medicine, patient-derived organoids, phosphoproteomics, imaging mass-cytometry

Background

In the past two decades, tremendous advances have been made in both cancer biology by identifying recurrent mutations in oncogenic signaling pathways using sequencing technologies and therapeutics by developing targeted drugs specific for these mutations. In colorectal cancer (CRC), one of the major cancers with high incidence and where mortality rates are still high [1], progress in targeted therapy has been limited, relative to other solid cancers like lung cancer or melanoma [2]. The genetic heterogeneity [3] as well as paucity of druggable targets (nearly 50% of all CRCs are driven by undruggable oncogenes of the *RAS* family) [2] pose considerable challenges for developing precision oncology approaches for patients with CRC. Moreover, CRC seems to be refractory to therapy with immune checkpoint blockers (ICB) with the notable exception of CRC tumors characterized by mismatch-repair deficiency or POLE proofreading mutations [4]. This is somehow paradoxical since CRCs, irrespectively of mismatch repair status, are known to be under immunological control, as we have shown in the past [5].

In precision oncology the paradigm is emerging that genomic profiling of the tumor assessed at early intervention (biopsy or resection) does not provide sufficient information to guide therapy. A diagnostic approach that is functional, i.e. measuring responses to perturbations with living cells derived from the specific tumor is expected to provide immediately translatable, personalized treatment information [6]. Such functional precision medicine approach requires patient derived models representing the tumors from affected individuals like patient-derived xenografts (PDX) or patient-derived organoids (PDOs) [7]. However, despite earlier encouraging reports [8,9], conflicting results have been reported regarding the capability of PDOs to predict tumor responses to specific drugs [10] Moreover, a recent study showed that despite sensitivity of the PDOs to selected kinase inhibitors, CRC patients from which these cells originated did not demonstrate objective clinical response to the treatment [11]. A number of reasons can be attributed to the limited value of PDOs as a tool for functional precision oncology. These include PDO culture success rate, ineligibility of the patients, or limited set of drugs tested [11]. While improvements for more streamlined experimental design are conceivable and could accelerate the implementation of PDOs to guide treatment decisions, major limitations of this drug-screening approach remain. The read-outs of the assays for testing *in vitro* response are based on growth rates of the cells and do not measure changes in the levels of functional status of the corresponding proteins and hence, do not provide insights into the mechanisms underlying sensitivity or resistance to a specific drug. Moreover, given the large number of available approved drugs, testing existing drugs for novel therapeutic strategies (drug repurposing) or testing novel combinations even for a limited number of single agents becomes impractical. Thus, an improved approach is needed that identifies key cancer cell vulnerabilities and provides rationale to select drugs/drug combinations. Given the fact that dysfunctional signaling in tumors arises from rewiring of signaling pathways and

that nearly all molecularly targeted therapeutics are directed against signaling molecules [12], a strategy that focuses on cancer cell signaling measurements in PDOs could offer an alternate road forward.

Such a functional precision oncology strategy based on comprehensive dissection of tumor cell signaling depends on obtaining quantitatively accurate and consistent phosphoproteomics profiles. Recently, data-independent acquisition (DIA) methods emerged as a technology that combines deep proteome coverage with quantitative consistency and accuracy. Specifically, a variant of DIA methods called sequential window acquisition of all theoretical mass spectra (SWATH-MS)[13] was developed in which all ionized peptides within a specified mass range are fragmented for each sample in a systematic manner [14], and thereby enable reproducible high-throughput identification and quantification of proteomes across many samples. We reasoned that functional precision profiling using PDOs and SWATH-MS-based quantitative phosphoproteomics would enable patient-level reconstruction of kinase signaling networks and shed light on the intrinsic biology of the CRC cells.

We therefore first established a living biobank of PDOs from CRC patients and carried out steady-state proteogenomic characterization using DNA- and RNA-sequencing, and SWATH-MS-based proteomics (Figure 1). We then developed a functional precision oncology approach based on perturbation experiments of the PDOs with kinase inhibitors, quantitative phosphoproteomic measurements, and integration of *a priori* knowledge. We show that kinase inhibitors induce profound off-target effects that impact oncogenic and immune-related pathways. Reconstruction of the topologies of kinase signaling networks showed that patient-specific rewiring is largely unaffected by mutations. Moreover, we show non-genetic heterogeneity of the PDOs and upregulation of stemness and differentiation genes by kinase inhibitors. Finally, we complemented our functional precision profiling by imaging mass cytometry (IMC)-based analysis of the primary tumors that enabled us to quantify spatial heterocellular crosstalk and tumor-immune cell interactions.

Methods

Human specimens

Histologically verified primary and metastatic colorectal tumor tissues and blood samples were obtained from patients undergoing surgical resection at the Medical University Hospital of Innsbruck. Samples were obtained from adult female or male patients who were treatment-naïve, with the exception of patient CRC26 who received FOLFOX and cetuximab before surgery. Written informed consent for research was obtained from patients prior to tissue acquisition. The medical ethical committee of the Medical University of Innsbruck approved protocol AN2016-0194 366/4.9 for the establishment of colorectal cancer PDOs cultures.

Tumor cells isolation

Tumors were washed three times with DPBS (Thermo Scientific, Cat#14190169) containing 100 µg/ml Primocin (Invivogen, Cat#ant-pm-2) and 10 ml/L Penicillin-Streptomycin (Sigma, Cat#P4333), minced finely and incubated with 25 ng/ml Liberase (Roche, Cat#5401054001) in StemPro hESC SFM (Thermo Scientific, Cat#A1000701) for 1 hour at 37°C. After incubation, StemPro hESC SFM containing 10% FBS (Sigma, Cat#F7524) was added and the mixture was put over a 400 µM and a 100 µM cell strainers (pluriSelect, # 43-50100-51 and 43-50400-03) to remove large fragments. Cells were spun at 1000 rpm for 4 minutes, pellet was resuspended in 1x RBC Lysis Buffer (Biolegend, Cat#B420301) and incubated for 10 minutes at room temperature. Cells were spun at 1500 rpm for 5 minutes and pellet was washed three times with DPBS followed by centrifugation at 1500 rpm for 3 minutes.

PDOs culture

Isolated tumor cells were seeded at a density of $1.5x10^5$ in 30 µl droplets of 70% Geltrex (Thermo Scientific, Cat#A1413202). The composition of PDO culture medium was: Advanced DMEM/F12 (Thermo Scientific, Cat#12634028) supplemented with 10 mM Hepes solution (Sigma, Cat#H0887), 10 ml/L Penicillin-Streptomycin solution, 2 mM GlutaMAX (Thermo Scientific, Cat#3550061), 20% Rspondin conditioned medium, 10% Noggin conditioned medium, 20 ml/L B-27 supplement (Thermo Scientific, Cat#17504044), 1.25 mM N-Acetylcysteine (Sigma, Cat#A9165), 0.5 nM A83-01 (Tocris, Cat#2939), 10 µM SB202190 (Sigma, Cat#S7067), 50 ng/ml human EGF (Peprotech, Cat#AF-100-15), 100 µg/ml Primocin (Invivogen, Cat#ant-pm-2), and 10 µM Y27632 (AbMole, Cat#M1817). PDO culture medium was refreshed every two days. To passage the PDOs, Geltrex was broken with a cell scraper and PDOs were collected in a tube. The PDOs were centrifuged at 1500 rpm for 5 minutes, medium was removed, the pellet was resuspended in TripLE Express (Thermo Scientific, Cat#12604013) and incubated for 5 minutes at 37°C. Advanced DMEM/F12 was added and cells were spun down at 1500 rpm for 5 minutes. The pellet was resuspended in 70% Geltrex and plated in 30 µl

droplets on 6 wells-plates (Sarstedt, #83.3920), 4 drops each well. After allowing Geltrex to solidify, PDO culture medium was added to the plates and PDOs were incubated at 37°C with 5% CO2.

Perturbation experiments with PDOs

PDOs were cultured and expanded to forty-eight 30µl culture-droplets for each condition. At 2 hours before collection, PDOs were treated with single inhibitors (or DMSO as solvent control) or at 1 hour before collection were stimulated with ligand (or solvent control H2O). The following inhibitors and ligand were used as previously evaluated [15]: MEKi AZD6244 (4 µmol/L, Biomol, #LKT-S1846.1), PI3Ki AZD6482 (10 µmol/L, Biomol, #Cay15250-1), mTORi AZD8055 (2 µmol/L, Eubio, #SYN-1166-M001), TBK1i BX-795 (10 µmol/L, Sigma, #SML0694), BRAFi PLX4720 (5 µmol/L, Biomol, #Cay15142-1), TAK1i 5Z-7-Oxozeaenol (5 µmol/L, Sigma, O9890), and TNFα (10 ng/mL, Peprotech, AF-300-01). After treatment, cultivation dishes were placed on ice and PDOs culture-droplets were washed twice with ice-cold DPBS. Culture-droplets were disrupted in Cell Recovery Solution (Corning, #7340107), collected in a tube and incubated for 1 hour on ice. After incubation, PDOs were spun at 1500 rpm for 10 minutes at 4°C, washed twice with ice-cold DPBS and PDO pellets were snap-frozen in liquid nitrogen and stored at -80°C.

PDOs preparation for proteomics analysis

PDOs were cultured and expanded to six 30µl culture-droplets for each sample. At the time of collection, cultivation dishes were placed on ice and PDOs culture-droplets were washed twice with ice-cold DPBS. Culture-droplets were disrupted in Cell Recovery Solution (Corning, #7340107), collected in a tube and incubated for 1 hour on ice. After incubation, PDOs were spun at 1500 rpm for 10 minutes at 4°C, washed twice with ice-cold DPBS and PDO pellets were snap-frozen in liquid nitrogen and stored at -80°C.

DNA and RNA sequencing

PDOs were harvested, snap-frozen and their DNA were extracted using the PureLink Genomic DNA Mini Kit (Thermo Scientific, #K182001) following manufacturer instructions. Germline DNA were extracted from frozen peripheral blood mononuclear cells (PBMCs) using PureLink Genomic DNA Mini Kit (Thermo Scientific, #K182001) following manufacturer instructions. RNA was isolated from PDO pellets using the RNeasy Plus Mini Kit (Qiagen, #74134) following manufacturer instruction. Exome-sequencing was performed using SureSelect all human V6 capture kit and Illumina sequencing (GATC, Konstanz, Germany and GENEWIZ, Leipzig, Germany). Total RNA was isolated from frozen PDO pellets using the RNeasy Plus Mini Kit (Qiagen, #74134) following manufacturer's instruction and submitted to total transcriptome full-length mRNA sequencing (GATC, Konstanz, Germany, Medical University of Innsbruck).

Single cell sequencing

PDO culture-droplets were washed once with warm DPBS, disrupted with a cell scraper and collected in a tube followed by centrifugation at 1500rpm for 5 minutes at room temperature. PDO pellets were resuspended in Trypsin-EDTA (Sigma, Cat#T4174) using 500 µl for each culture-droplet used, resuspended 5 times with a 1000µl tip and incubated for 5 minutes at 37°C. An equal volume of Advanced DMEM/F12 was added and PDOs were further dissociated mechanically by resuspending 10 times using a 200 µl pipette tip placed on top of a 1000 µl tip. Cells were filtered through a 40 µm cell strainer and centrifuged at 1500rpm for 5 minutes at 4°C. Supernatant was removed and cell pellets were resuspended in 1 ml ice-cold 0.04% BSA in DPBS. Cells were counted with a hemocytometer (Marienfeld Neubauer, Cat#0640010) and viability was assessed using Trypan-blue solution (Sigma, Cat#T8154). Single cell suspensions of freshly isolated cells were converted to indexed scRNAseq libraries, using the Chromium Single Cell 3'GEX V3.1 technology from 10x Genomics, aiming for 8.000 cells per library. The resulting Libraries were sequenced with Illumina Novaseq technology (sequencing performed at Genewiz, Leipzig, Germany).

Immunofluorescence

PDO samples for immunofluorescence were prepared as described [16]. Briefly, PDOs were freed from Geltrex by incubation in Cell Recovery Solution (Corning, #7340107) for 1 hour on ice, fixed in 4% PFA (Sigma, #16005) in PBS for 1 hour at RT and permeabilized in 1% Triton X-100 (Sigma, #T9284) for 30 minutes at RT. PDOs were incubated in Blocking Buffer (10% goat serum (Sigma, #G9023), 0.2% Triton X-100, 5% BSA in PBS) for 1 hour at RT and with primary antibodies in Blocking Buffer overnight at 4°C. PDOs were washed twice with PBS, incubated with secondary antibodies in Blocking Buffer for 2 hours at RT in the dark, washed twice with PBS and mounted in Vectashield Antifade Mounting Medium with DAPI (#H-2000-2). Following primary antibodies were used: anti-chromogranin A (Santa Cruz Biotechnology, #sc-393941, 1:500), anti-lysozyme (Abcam, #ab108508, 1:500), anti-mucin 2 (Santa Cruz Biotechnology, #sc-515032, 1:500), anti-EpCAM (R&D, #AF960-SP, 1:20), anti-Ki67 (Abcam, #ab92742, 1:500), anti-Lgr5 (Abcam, #ab75732, 1:100), anti-SOX9 (Sigma, #AB55351:500), Phalloidin-iFluor 647 (Abcam, #ab176759, 1:1000). All secondary antibodies were used 1:800. Immunofluorescence images were captured with an Operetta CLS High-Content Analysis System (Perkin Elmer).

Western blotting

PDOs were lysed in RIPA buffer with 1x EDTA-free protease inhibitor cocktail (Sigma, #11836170001), 1% v/v phosphatase inhibitor cocktail (Sigma, #P0044) and 2mM PMSF (Sigma, #93482). Protein concentration was measured by BCA Protein Assay Kit (Thermo Scientific, #23225), proteins were separated on 7%, 10% or 12% precast polyacrylamide gels (NuPAGE) following the manual. Blotting was performed using the Invitrogen™ Novex™ XCell™ SureLock™ Blot-Modul

(Invitrogen) according to the manufacturer instructions. Following primary antibodies were used according to manufacturer's protocol: GAPDH (Santa Cruz Biotechnology, #sc-47724, 1:1000 and Invitrogen, #AM4300, 1:10000), phospho-mTOR (Cell Signaling, #5536T, 1:2000), phospho-AKT (Cell Signaling, #4060S, 1:1000), phospho-ERK1/2 (Cell Signaling, #4377S, 1:1000), phosho-MEK1 (Invitrogen, #MA-32165, 1:1000), phospho-p38 MAPK (Invitrogen, #36-8500, 1:1000. Chemiluminescence was recorded using the Image Quant Las4000 imaging system (GE Healthcare).

mRNA expression analysis of selected genes by RT-qPCR

PDOs were cultured in 6 well flat bottom plates and treated with kinase inhibitors (5 µM BRAFi , 4µM MEKi, 2µM mTORi, 10µM PI3Ki, 5µM TAKi, 0.25 µM TBKi) and vehicle control (DMSO) for 72 hrs. After the treatment, organoid pellets were harvested by washing twice in cold PBS, snap frozen in liquid N2 and stored at -80°C before RNA extraction. Total RNA was isolated using RNeasy Plus Mini Kit (Qiagen, cat#: 74134). cDNA was synthesized using SuperScriptIII first-strand synthesis system for RT-PCR (Invitrogen) with 1µg of total RNA as a template. Quantitative PCR (qPCR) was performed in MicroAmp™ Optical 384-Well Reaction Plates with Barcode (Applied Biosystems, cat#: 4309849) on ViiA™ 7 Real-Time PCR System (Applied Biosystems) using Platinum™ SYBR™ Green qPCR SuperMix-UDG w/ROX (Invitrogen, cat#: 11744500). The final volume for qPCR reaction was 6µl containing 4ng of cDNA, 0.2µM of each primer and 1X Platinum™ SYBR™ Green qPCR SuperMix. Cycling conditions for qPCR were as follows: 2 mins at 50°C, 10 mins at 95°C followed by 40 cycles of 15 s at 95°C and 60 s at 60°C. Primers used for qPCR are listed in Table S1.

Sample preparation for mass spectrometric analyses

Pelleted and frozen PDOs were lysed in 8 M Urea (Sigma, #33247) in 100 mM ammonium bicarbonate (Sigma, #09830) and with sonication for 10 min. For the perturbation experiments, 1:100 phosphatase inhibitor cocktails (Thermo Scientific #P5726 and Sigma #P0044) were added to the lysis buffer. To reduce and alkylate the disulfide bonds, the lysate was reduced using 5 mM tris(2-carboxyethyl)phosphine (TCEP) for 30 min at 37°C and alkylated using 40mM Iodacetamide (IAA) for 45 min at 25°C in the dark. The protein amount was measured using the Bicinchoninic acid (BCA) assay (Thermo Scientific, #23225) and the appropriate protein amount (60 µg for baseline expression experiments and 1mg for perturbation experiments) was digested with LysC (1:100, Wako, #121-05063) for 4 h and Trypsin (1:75, Promega, #V5113) overnight. For the digestion with LysC and Trypsin, the samples were diluted to 6 M and 1.5 M Urea (Sigma, #33247) in 100mM ammonium bicarbonate respectively using 100 mM ammonium bicarbonate (Sigma, #09830). The digestion was stopped the following day by acidification with trifluoroacetic acid to pH 2-3.

For the baseline expression experiments, the digested peptides were desalted using NEST C18 MicroSpin™ columns by washing with 2% acetonitrile 0.1% trifluoroacetic acid and eluting with 50% acetonitrile 0.1% trifluoroacetic acid. The eluted peptides were dried in a vacuum concentrator, reconsti-

tuted in 60µl 2% acetonitrile 0.1% formic acid in H2O, and spiked with iRT peptides (Biognosys, #Ki-3002-1) prior to injection into the mass spectrometer.

For the perturbation experiments, the digested peptides were desalted using Waters Sep-pak C18 columns by washing with 0.1% trifluoroacetic acid in H2O and eluting with 50% acetonitrile and 0.1% trifluoroacetic acid in H2O. The eluted peptides were subsequently dried in a vacuum concentrator. Before drying fully, an aliquot (1:20) was taken for the corresponding total cell lysate samples. The aliquot was dried and the peptides were dissolved in 2% acetonitrile and 0.1% formic acid in H2O and spiked with iRT peptides (Biognosys, #Ki-3002-1) prior to injection into a mass spectrometer. The remaining part of the sample was destined for phosphoenrichment and dried in a vacuum concentrator.

To enrich for phosphopeptides, the peptides were first dissolved in a tube with loading buffer (1 M glycolic acid, 5% trifluoroacetic acid, 80% acetonitrile in H2O) by shaking 10 min and sonicating for 10 min. For phosphoenrichment, stage tips were constructed placing two C8 plugs into an empty 300 µl tip. These stage tips were placed in a tube using a connector and centrifuged on a table top centrifuge at around 800 g for all subsequent washes. The stage tips were washed with 200 µl methanol to condition the filter. To the washed tips, 80 µl TiO2 bead slurry (2.5 mg TiO2 beads in 50% acetonitrile, 0.1% trifluoroacetic acid) were added and the beads were equilibrated with 200 µl loading buffer. The peptides were loaded by starting with a low centrifugation force of 100 g that was progressively increased until all peptides were loaded. The loaded peptides were washed once with 100 µl loading buffer, once with 100 µl 80% acetonitrile and 0.1% trifluoroacetic acid in H2O, and once with 100ul 50% acetonitrile and 0.1% trifluoroacetic acid in H2O. The peptides were eluted with 250 µl 0.3 M NH3OH and a subsequent elution of 20 µl 50% acetonitrile and 0.1% trifluoroacetic acid in H2O to elute peptides from the filter paper. The phosphopeptides were eluted directly in a tube with trifluoroacetic acid to reach pH 2. The phosphopeptides were then desalted using NEST UltraMicroSpinTM C18 columns and eluted with 50% acetonitrile, 0.1% trifluoroacetic acid in H2O. The buffer was evaporated in a vacuum concentrator and the peptides were dissolved in 2% acetonitrile and 0.1 % formic acid in H2O and spiked with iRT peptides (Biognosys, #Ki-3002-1) prior to injection of samples into a mass spectrometer.

Acquisition of samples using mass spectrometry

For the perturbation experiments, the peptides were analyzed on an Orbitrap Fusion Lumos mass spectrometer (Thermo Scientific, San Jose, CA) connected to an Easy-nLC 1200 (Thermo Scientific, San Jose, CA) HPLC system. Between 1 µl and 4 µl of peptide solution was separated by nano-flow liquid chromatography using a 120 min gradient from 5 to 37% buffer B in buffer A (Buffer A: 2% acetonitrile, 98% H2O, 0.1% formic acid; Buffer B: 80% acetonitrile, 20% H2O, 0.1% formic acid) on an Acclaim PepMap RSLC 75 µm x 25cm column packed with C18 particles (2 µm, 100 Å) (Thermo Scientific, San Jose, CA). The peptides were ionized using a stainless steel nano-bore emitter (#ES542; Thermo Scientific) using 2000 V in positive ion mode.

To build the spectral libraries, the samples were acquired in data-dependent acquisition (DDA) mode. The DDA method consisted of a precursor scan followed by product ion scans using a 3 s cycle time. The precursor scan was an Orbitrap full MS scan (120’000 resolution, 2 × 105 AGC target, 100 ms maximum injection, 350-1500 m/z, profile mode). The product ion scans were performed using Quadrupole isolation and HCD activation using 27% HCD Collision Energy. The Orbitrap was used at 30’000 resolution and setting the RF Lens at 40%. The AGC Target was set to 5 × 105 and 50 ms maximum injection time. Charge states of 2-5 were targeted and the dynamic exclusion duration was 30s.

To quantify the peptide abundance, the samples were acquired in data-independent acquisition (DIA) mode. The DIA method consisted of a precursor scan followed by product ion scans using 40 windows between 400 m/z and 1000 m/z. The precursor scan was an Orbitrap full MS scan (120,000 resolution, 2 × 105 AGC target, 100 ms maximum injection, 350-1500 m/z, profile mode). The product ion scans were performed using Quadrupole isolation and HCD activation using 27% HCD Collision Energy. The Orbitrap was used at 30,000 resolution using a scan range between 200 and 1800 and setting the RF Lens at 40%. The AGC Target was set to 5 × 105 and 50 ms maximum injection time.

For the baseline expression experiments, the peptides were measured on a Sciex TripleTOF 5600 mass spectrometer with a 90 min gradient and the mass spectrometer was operated in SWATH mode. The precursor peptide ions were accumulated for 250 ms in 64 overlapping variable windows within an m/z range from 400 to 1200. Fragmentation of the precursor peptides was achieved by Collision Induced Dissociation (CID) with rolling collision energy for peptides with charge 2+ adding a spread of 15eV. The MS2 spectra were acquired in high-sensitivity mode with an accumulation time of 50 ms per isolation window resulting in a cycle time of 3.5 s. The samples from the different PDOs were injected consecutively in a block design to prevent any possible confounding effects due to deviation in machine performance. CRC03 and CRC26 were acquired at a later time point, but some original samples were reinjected in parallel to assess that the performance of the machine was similar.

Building the spectral library for the perturbation experiments

The raw spectra were analyzed using MaxQuant version 1.5.2.8 that matched each spectrum against a FASTA file containing 20,386 reviewed human (downloaded on August 13, 2018 from www.uniprot.org) and iRT peptides and enzyme sequences. Carbamidomethyl was defined as a fixed modification, and Oxidation (M) as variable modifications. Standard MaxQuant settings for Orbitrap were used (e.g. peptide tolerance 20 ppm for first search and 4.5 for main search). In total, two searches were performed involving 54 injections of peptides and they resulted in the identification of 42’424, peptides from 4’239 protein groups, respectively. The four searches were imported into Spectronaut Pulsar (version 14.0.200309.43655 (Copernicus) Biognosys, Schlieren) to build spectral libraries with the following settings: PSM FDR Cut off of 0.01, fragment m/z between 200 and 1’800, peptides with at least 3 amino acids, fragment ions with a relative intensity of at least 5, precursors with at

least 5 fragments. Moreover, an iRT calibration was performed with a minimum root mean square error of 0.8 and segmented regression. The spectral library for the total cell lysates contained coordinates for 54'551 precursor peptides from 4'223 protein groups. The spectral library for the phosphopeptide contained coordinates for 30'969 precursor peptides from 4'605 protein groups.

Extraction of quantitative data from the mass spectrometry spectra

For the perturbation experiments, quantitative data were extracted from the acquired SWATH-MS maps using Spectronaut Pulsar (version 14.0.200309.43655 (Copernicus) Biognosys, Schlieren) (version 14). As SWATH Spectral library, we used our in-house compiled spectral libraries for the PDOs (see above). We used standard settings (they include a dynamic MS1 and MS2 mass tolerance strategy, a dynamic XIC RT Extraction Window with a non-linear iRT calibration strategy, and identification was performed using a precursor and protein Q value cutoff of 0.01). The quantified intensities for each fragment were extracted from 104 (phospho-enriched samples), 99 (total cell lysate) SWATH-MS injections and the fragment intensities were exported for further statistical analysis to R. Only quantities for fragments that have been detected at least two times in a given condition were selected. Further filtering was performed with mapDIA where a standard deviation factor of 2 and a minimal correlation of 0.25 were used to filter for reliable fragments.

For the baseline expression experiments, the SWATH-MS data was quantified using the OpenSWATH workflow on the in-house iPortal platform using the PanHuman Library [17]. An m/z fragment ion extraction window of 0.05 Th, an extraction window of 600 s, and a set of 10 different scores were used as described before. To match features between runs, detected features were aligned using a spline regression with a target assay FDR of 0.01. The aligned peaks were allowed to be within 3 standard deviations or 60 s after retention time alignment. The data was then further processed using the R/Bioconductor package SWATH2stats.

Variant calling, Copy Number Variation and Neoantigen prediction

Somatic mutations, copy number alterations, Class I and II HLA types and neoantigens were called by running our previously published neoantigen prediction pipeline nextNEOpi [18] (version 1.1).

Briefly, we used the pipelines default options but enabled automatic read trimming to remove adapter sequence contamination from raw WES and RNAseq reads and we disabled NetChop and NetMHCstab. Further, we created a panel of normals from the healthy PBMCs and used it to identify recurrent technical artefacts in order to improve the results of the variant calling analysis. Finally, predicted neoantigens were filtered and prioritized using the "relaxed" filter set from nextNEOpi.

The MSI status was determined with MSIsensor [19] and the scores were plotted as bar plots.

RNA-sequencing data analysis

Sequence reads were preprocessed and mapped to the human genome GRCh38/hg38 and GENCODE v33 annotations using the nf-core RNAseq pipeline version 1.4.2 (git revision ff4759e)[20]. In brief, reads were mapped using STAR v2.7.1a [21] and gene expression quantified with RSEM v1.3.3 [22]. Pathway activity scores were estimated from normalized raw counts using the PROGENy (Pathway RespOnsive GENes) method [23]**.** GO enrichment analysis was performed using the R package ClusterProfiler 4.1.0 [24]. Eight major clusters were defined and annotated by the GO enrichment results. Heatmaps for visualization of RNAseq results were generated using the ComplexHeatmap 2.9.0 R package [25].

Single-cell RNA-sequencing data analysis

The single-cell RNA sequencing reads were mapped to GRCh38-2020-A reference provided by 10x Genomics using the CellRanger pipeline (v5.0.0). Cellranger's pre-filtered count matrices were loaded into scanpy [26] and filtered based on the following quality control cutoffs: $\geq$ 2000 genes, 2000 $\leq$ counts $\leq$ 75,000, < 25% mitochondrial reads. Doublets were removed using SOLO [27] v0.6.0. The 5000 most highly variable genes (HGVs) were detected with *scanpy.highly_variable_genes* with *flavor="seurat_v3"* and *batch_key="organoid"*. Batch effects were removed using scvi-tools v0.11.0 [28] based on the HVGs and using PDOs as the batch key. A neighborhood graph and UMAP embedding [29] were calculated with scanpy based on the SCVI latent representation and otherwise default parameters. Unsupervised clustering with the leiden-algorithm [30] based on the SCVI-corrected neighborhood graph (resolution=0.5) yielded 12 clusters. Marker genes for each cluster were detected using scvi-tools differential gene expression module [31] and clusters manually assigned to 7 epithelial cell-types based on these marker genes. For visualization, gene expression was CPM-normalized and log1p-transformed, before computing an additional (uncorrected) neighborhood graph and UMAP embedding. RNA velocity was estimated using velocyto.py (v0.17.17) [32] based on cellranger outputs using the *run10x* command and subsequently loaded into scvelo [33] for visualization. We performed single-cell pathway analysis using PROGENy [23,34]. Scores were computed using the *progeny-py* package v1.0.6. The top 1,000 target genes of the progeny model were used, as recommended for single-cell data.

Proteomic data analysis

After quality control steps the median intensity value of baseline proteomic triplicates was retrieved for downstream analysis. Non-uniquely identified proteins were also discarded from further analyses. Differential abundance analysis was done using mapDIA version 3.1.0 [35]. Single-sample enrichment analysis of baseline protein expression levels was performed with the GSVA R package version 1.42.0 [36] using HALLMARK gene sets (version 7.5.1) imported with msigdbr 7.5.1 from MSigDB [37]. All samples, including replicates were transformed to log2 scale and resulting enrichment scores were then averaged per organoid. GO enrichment analysis was performed the same way as for the RNAseq

data (8 major clusters). Heatmaps for visualization of proteomics results were generated using the ComplexHeatmap 2.9.0 R package [25].

Correlation between mRNA and protein abundance

In total, the dataset comprises 3723 overlapping genes and proteins, but only those which were present in at least four out of the 12 matching samples were considered for correlation analysis (n=3536). Log2 transformed TPM-values for mRNA and log2-transformed protein abundances were used to calculate the Pearson correlation coefficient for each gene. The average correlation between mRNA and protein abundance is 0.29. The results were visualized in a histogram using the ggplot2 R package.

Protein complexes

The list of manually curated protein complexes was retrieved from Ori et al [38]. Human protein complexes with a minimum of five proteins were selected and Pearson correlations within complexes were calculated across PDOs. The top 25% of the protein complexes were considered as variable, whereas the bottom 25% were defined as stable protein complexes. For the 26S proteasome the variance was calculated for all members of the complex, ignoring missing values. The results were visualized as a barplot using the ggplot2 R package.

Phosphoproteomic data analysis

Phosphopeptide fragment data were prefiltered for intensities above 2000 and peptides with at least five measured fragments. Missing replicate values were replaced by the 20% value of the minimum of the corresponding fragment abundance. Differential abundance analysis was done using mapDIA version 3.1.0 [35]. Protein sequences and gene symbols were retrieved from UniProt [39] using the UniProt.ws 2.36.5 R package. Phosphopeptide sequences were matched to protein sequences to determine phosphosite positions. If multiple phosphopeptides mapped to the same phosphosite, we selected the site with the higher mean signal in control samples. Phosphosite readouts for kinases directly targeted by the inhibitors we used were taken from the SIGNOR 2.0 database [40]. Posttranslational modification set enrichment analysis (PTM-SEA) was performed using the ssGSEA 2.0 R script (ssgsea-cli.R) and the PERT-, PATH- and KINASE-signature categories of the PTMsigDB v1.9.0 database [41] and kinase/phosphatase signatures derived from SIGNOR. We used fold-change-signed log10-transformed FDR values from mapDIA as input scores and protein-centric phosphosite positions as identifiers. Peptides with multiple phosphorylated residues were demultiplexed as suggested in the original publication. Normalized enrichment scores (NES) and global false-discovery-rate-adjusted p-values (FDR) were calculated with the number of permutations set to 100000, “area.under.RES” as the test statistic, a weight of one, no additional normalization and a minimum overlap of two measured sites per signature. Heatmaps for visualization of phosphoproteomics results were generated using the Complex-

Heatmap 2.9.0 R package [25]. The numbers of shared differential abundant phosphopeptides were visualized in R with the UpSetR package.

Kinase signaling network analysis

Network analysis and visualization was performed with the igraph 1.3.2 [42], tidygraph 1.2.1 and ggraph 2.0.5 R packages. We mapped normalized enrichment scores of kinase signatures from PTMsigDB to nodes and phosphosite log-fold-changes to edges of the global human SIGNOR 2.0 signaling network (retrieved on 23.04.2021) [40]. Perturbation subnetworks were identified from perturbed nodes (kinase signature FDR <= 0.05) and perturbed edges (phosphosite FDR <= 0.05). Briefly, we calculated all shortest paths with a maximum length of two edges between perturbed nodes, combined them with perturbed edges and filtered for the largest connected component. The subnetworks were further refined by pruning them of redundant shortest paths according to whether they could be annotated with measured phosphosites. We further combined the resulting treatment-specific subnetworks into PDO-specific networks, calculated degree and eigenvector centralities of all nodes and tested for overrepresentation of coding mutations using a two-sided Fisher's Exact Test.

Imaging mass cytometry

Four µm tissue sections were placed on silane-coated glass slides, dried overnight at 37 °C and stored at 4 °C. Carrier-free IgG antibodies (Table S2) were conjugated to purified lanthanide metals with the MaxPar antibody labeling kit and protocol (Fluidigm) as described by Ijsselsteijn et al [43]. Imaging mass cytometry immunodetection was performed following the protocol described previously by Ijsselsteijn et al [43]. In short, tissue sections were deparaffinized through immersion in xylene for 3 times 5 minutes and rehydrated in decreasing concentrations of ethanol. 10x low pH antigen retrieval solution (Thermo Scientific, #00-4955-58) was diluted in purified water and preheated for 10 minutes in a microwave. The sections were rinsed in unheated 1x low pH antigen retrieval solution, boiled for 10 minutes in the preheated buffer and cooled down to room temperature for 1 hour. Sections were rinsed with PBS-TB (PBS supplemented with 0,05% Tween and 1% BSA) and incubated for 30 minutes with 200µl Superblock blocking buffer (Thermo Scientific, #37515). Antibody incubation was split into two steps: a 5 hour incubation at room temperature and an overnight at 4 °C incubation. The antibody mix for the 5 hour incubation was prepared by diluting the first half of antibodies (Table S2) in PBS-TB after which 100µl of antibody mix was added to the tissue sections and incubated for 5 hours at room temperature in a humid chamber. The sections were washed three times for 5 minutes with PBS-TB and incubated overnight at 4 °C in a humid chamber with the remaining antibodies (Table S2) diluted in PBS-TB. The sections were washed three times with PBS-TB and incubated for 5 minutes at room temperature with 100µl Intercalator Ir (1,25µM diluted in PBS-TB). Tissue sections were washed two times for 5 minutes with PBS-TB and once with purified water for 5 minutes. Finally, the sections were dried under an air flow and stored at RT until ablation. For each tissue, 8 re-

gions of interest were chosen based on hematoxylin and eosin staining on consecutive sections that were representative for the whole tissue. The Hyperion imaging mass cytometry system (Fluidigm) was calibrated using a 3-element tuning slide (Fluidigm) following the manufacturers settings with an extra threshold of 1500 mean duals detected for 175Lu. In total, 40 ROIs of 1000x1000µm were ablated after which 3 ROIs were excluded due to poor quality.

Imaging mass cytometry data analysis

Data was exported as .MCD files and for each ROI color TIFF images were created containing the DNA, vimentin and keratin signal using the Fluidigm MCD viewer. These were used to segment the images into nucleus, membrane and background using a random forest classifier in Ilastik [44]. The exported probability maps were used to create cell masks in cell profiler [45]. Simultaneously, the MCD files were transformed to .OME.TIFF files using the Fluidigm MCD-viewer. In Ilastik, pixels were assigned to either 'signal' or 'background' per marker to train a random forest classifier, which was applied to the entire dataset. Data was exported as binary segmentation masks for each marker where the 'background' pixels were set to 0 and the 'signal' pixels to 1. These signal masks together with the cell masks and ome.tiff files were loaded into ImaCytE [46] to create FCS files containing per cell the mean pixel intensity for each marker. HSNE clustering on the FCS files of all images was performed in Cytosplore [47] to generate phenotype clusters which were mapped back onto the images in IMACyte. Each cluster was visually confirmed using the original .MCD files and combined when similar clusters were observed. The phenotype clusters were further processed using R to calculate cell densities (cells/mm2), composition of present immune cells and to investigate the expression of selected markers of interests in specific phenotype clusters for each sample. Threshold of 10% was set for the marker values, i.e. a cell is considered as positive for a certain marker if in at least 10% of its area the marker was positively detected. The Spearman pairwise correlation heatmaps of cell phenotypes were also calculated for each sample separately. To assess the spatial organization and cell-cell interactions Voronoi diagrams were created and all cell-cell interactions (direct neighbors) were counted. To test whether the number of direct interactions of each pairwise cell type combination is significantly different than expected by chance, a Monte Carlo simulation with 1000 iterations was performed in which the location of the cells from the imaged slide was randomly permuted, while keeping the number of cells from each type constant and the overall cellular positions fixed. Then a z-score and p-value was calculated to assess avoidance or attraction (z-score < 2, z-score > 2, $p < 0.01$). A combined cohort z-score was then calculated using the Stouffer's z-score method for overall meta analysis and plotted as heatmaps (Figure S6). PD1+/PDL1+ microaggregates (min. 1 PDL1+ tumor cell and min. 1 PD1+ immune cell) were identified by finding connected components in a graph created from the Voronoi diagram. These microaggregates were color marked with the respective cell type colors and plotted as Voronoi diagrams (Figure 6A). To test if the number of PD1+/PDL1+ mi-

croaggregates per tumor was significantly different than expected by chance, we again performed a Monte Carlo simulation as described above and calculated z-scores and p-values (Table S3).

Results

Proteogenomic characterization of a living biobank

We generated and molecularly characterized a living biobank using organoid technology [48] (Supplementary Figure 1A) as the basis for the subsequent analyses. Tumor samples from 15 CRC patients, including microsatellite instable (MSI) and microsatellite stable (MSS) tumors were used to generate PDOs which were then characterized using exome-sequencing, transcriptome-sequencing, and SWATH-MS-based proteomics. Genomic characterization including CRC driver genes [49] and a panel of immune-related genes frequently mutated in CRC [50] reaffirmed previously reported somatic alterations [50] and showed that the biobank is representative of CRC (Figure 2A, Supplementary Figure 1B). As expected, MSS PDOs have few targetable mutations whereas mutations in immune-related genes including mutations in Human Leukocyte Antigen (HLA) class I and class II genes were almost entirely detectable in MSI PDOs (Figure 2A). WNT signaling (*CTNNB1* (ß-catenin)) and TGFß signaling genes (*SMAD2*, *SMAD4*) were mutated in both subtypes. We then predicted the presence of potential neoantigens including neoantigens derived from missense mutations and from fusion genes using RNA-seq data and our recently developed tool for predicting neoantigens [18] (Figure 2A). Both, HLA class I and class II-associated neoantigens from gene fusions were mostly detectable in MSS PDOs. Analyses of the neoantigen landscape showed that neoantigens from tandem duplications from acid ceramidase (*ASAH1*) were predicted in 25% of the PDOs, suggesting that this public neoantigen can be used for developing therapeutic vaccination using off-the-shelf vaccine for this CRC cohort.

Analysis of the steady-state transcriptomic data revealed expression of genes involved in chemokine-mediated signaling pathways, indicating possible crosstalk with immune cells (Supplementary Figure 1C). We then assembled a panel of genes associated with cancer immunity and immune evasion mechanisms including checkpoint molecules, antigen processing and presentation genes, specific chemokines and cytokines, and tumor cell-specific interferon γ-related (IFNγ) genes [51]. The expression of these genes was highly heterogeneous in the MSI and MSS samples with HLA class I genes showing increased expression in MSI relatively to MSS PDOs (Supplementary Figure 1D). Analysis of cancer pathways using transcriptomic data showed heterogeneous pathway activity and partitioning of the profiles in two main subgroups, one of which was predominantly MSI subtype related (Figure 2B).

Analysis of the protein expression data following SWATH-MS of the PDOs showed 3723 unique proteins across the samples (Supplementary Figure 1E). Pathway analysis using protein expression data showed partitioning related to the MSI and MSS subtypes (Figure 2C) with notable exception of CRC13 from the MSI group and CRC17 from the MSS group. Within the MSI group there was a ten-

dency for coordinated upregulation of the immune-related pathways, IFNα response, IFNγ response and IL2/STAT5 (Figure 2C). Gene-wise correlation analysis between RNA and protein expression (average gene-wise Pearson correlation 0.29, Figure 2D) showed that RNA expression is a poor predictor of protein expression for CRC driver genes and for immune-related genes.

As proteins generally exert their function in coordination with other proteins in cellular pathways complexed with other proteins [52,53], we analyzed the co-abundance for complex members of 78 complexes with at least 5 protein members across all PDOs (Table S4). Complexes with variable subunit composition included *TNFα*/*NFκB* signaling complex 7 and kinase maturation complexes 1 and 2 (Figure 2E). In our analysis, complexes with invariant subunit composition included spliceosome-A, mini chromosome maintenance (MCM) complex and 26S proteasome. However, within the 26S proteasome, large variability was observed for the protein complex subunits PSMB9 and PSMB8 of the immunoproteasome (Figure 2F), the expression of which is associated with immune response to ICBs in melanoma [54]. Noteworthy, the expression of PSMB9 was decreased in a large fraction of the organoids (Supplementary Figure 1F).

In summary, steady-state multi-omics profiling of the PDOs revealed molecular heterogeneity within the clinical subgroups of MSI and MSS tumors and showed a number of altered signaling pathways that could determine cellular responses to drug treatment. However, based solely on these multi-omic data, the identification of the mechanisms that shape key tumor vulnerabilities and determine response to targeted therapy remained elusive.

Functional precision profiling of PDOs reveals off-target effects and pathway crosstalk

In order to investigate the effects of the targeted drugs on specific pro-tumorigenic pathways as well as to identify potential signaling crosstalk with anti-tumorigenic pathways, we used perturbation experiments and quantitative phosphoproteomic profiling. We carried out perturbation experiments on selected PDO's using a panel of kinase inhibitors (BRAFi, MEKi, mTORi, PI3Ki, TAKi, TBKi, Supplementary Figure 2A) and one stimulus (TNFα) followed by RNA-sequencing and SWATH-MS phosphoproteomics measurements. SWATH-MS phosphoproteomics data of the signaling perturbation experiments was highly reproducible and comprised 10,664 phosphopeptides that were mapped to 7,778 unique phosphosites (Figure 3A, Supplementary Figure 2B). Unsupervised clustering of the identified phosphosites showed that the profiles were mostly specific for PDOs (Supplementary Figure 2C), suggesting patient-specific rather than treatment-specific phosphoproteomes. The overlap of the regulated phosphopeptides between the treatments was in the lower percentile range (Figure 3B) even for treatments with inhibitors targeting kinases in the same pathway (e.g. the inhibition of BRAF and MEK in the MAPK pathway).

We then analyzed 103 kinases using 508 phosphosites that matched phosphosites in a curated database of phosphosite-specific signatures (PTMsigDB) [41] (Table S5). The analysis revealed highly diverse responses to the perturbations in the PDOs and showed reduced activities of the targeted kinases including MAPK1, AKT1, CDK1, CDK2 upon treatment of the PDO's with the respective inhibitors (Figure 3C, Supplementary Figure 2D). However, there were extensive off-target effects of the inhibitors including activation of kinases in non-targeted cascades that were specific for both, PDOs and kinase inhibitors. For example, we observed an activation of mTOR following BRAF and TBK inhibition or activation of AURKB following mTOR inhibition in several PDOs (Figure 3C). Set enrichment analyses with the phosphosite-specific signatures (PTMsigDB) [41] revealed pathway crosstalk with a number of pathways including immune-related pathways, like IL-2, IL-6, and IL-33 pathway (Figure 3D). The pathway crosstalk was PDO- and inhibitor-specific and included increased and reduced pathway activity without any obvious pattern.

Rewiring of kinase signaling networks is mutation-independent

The observed off-target activation of kinases in non-targeted cascades and the resulting pathway crosstalk necessitates detailed characterization of the signal transduction network in order to identify optimal targets for effective modulation of the respective pathways. Signal transduction networks are highly adaptable and dynamic, the properties of which are primarily determined by the network topology [55]. In an attempt to reconstruct signaling networks in individual patients we developed a computational method using the phosphoproteomic data and *a priori* knowledge of protein-protein interaction networks (see Methods). Briefly, we assigned kinase activities to nodes and phosphosites to edges of the SIGNOR 2.0 signaling network [40]. To identify subnetworks probed by the perturbations with kinase inhibitors only nodes with differential kinase activity based on the enrichment score calculated using PTMSEA [41] and edges differentially phosphorylated were considered, and the largest module was extracted (see Methods). The individual subnetworks resulting from each perturbation were then amalgamated into a combined kinase signaling network for the corresponding PDO. The kinase signaling networks showed a large extent of heterogeneity with varying numbers of nodes and edges as well as kinase activities and target site phosphorylations (Figure 4A, Supplementary Figure 3). Strikingly, rewiring of the kinase signaling networks was largely independent of the mutations. We found no significant association of mutations with PDO networks (CRC02 pval=0.18, CRC03 pval=0.63, CRC04 pval=1.00, CRC13 pval=0.61, CRC26 pval=0.26, CRC26LM pval=1.00, Fisher's exact test;). In the 5 MSS PDOs harboring between 116 and 230 mutations (coding variants), there were zero (CRC03, CRC26LM), one (CRC04, CRC26) and two nodes (CRC02) with mutated proteins. Even in the MSI PDO (CRC13) with a large number of mutations (2850 coding variants) there was no significant association of the mutations with the edges in the signaling kinase network (pval=0.61).

It has been previously shown that node centrality values are correlated with the importance in maintaining network integrity [56]. We therefore performed comparative analysis of the kinase signaling networks for the PDOs and obtained centrality values for each kinase node. (Figure 4B). As expected, high centrality values were observed for targeted kinases (e.g. mTOR) and for the kinases in the central EGFR-RAS-MAPK pathway (e.g. MAPK1). However, additional nodes like PRKACA or PTPN7 had high centrality values, further supporting the notion of extensive off-target effects and pathway crosstalk.

Overall, using quantitative phosphoproteomic data from PDOs perturbed with kinase inhibitors we were able to reconstruct kinase signaling networks at the patient level. Albeit heterogenous between PDOs, the kinase signaling network topologies revealed intrinsic rewiring that was independent of the harboring mutations.

Single-cell analysis shows phenotypic and differentiation heterogeneity of PDOs

Our finding of non-mutational rewiring of kinase signaling networks suggests that non-genetic mechanisms like phenotypic plasticity and differentiation status of the tumor cells might have a larger impact on adapting the signaling circuitry and leading to disease phenotypes. According to the cancer stem cell hypothesis, tumors are organized in cell hierarchies similar to normal tissues, with stem cells at the apex, giving rise to transient amplifying (TA) progenitor cells that undergo differentiation into several cell lineages [57]. The revised cancer stem cells model postulates that cancer cells can dynamically shift between a differentiated state and a stem-like state [58], which in CRC is tightly linked to changes in Wnt-signaling. Noteworthy, disrupted differentiation is integral to colon carcinogenesis and is a regulator of cellular plasticity. Most CRCs are diagnosed as moderately differentiated [59] with some cell types being implicated in therapy response. For example, it has been shown that enteroendocrine progenitors support *BRAF*-mutant CRC [60]. Hence, it appears that the hierarchically organized tumor cell heterogeneity and cell plasticity play key roles in both, CRC progression and therapy response as shown recently [61]. We therefore aimed to determine the hierarchically organized tumor cell heterogeneity in our PDOs and employed single-cell RNA sequencing.

We generated transcriptomic profiles from 37,924 cells (after quality control and filtering) which clustered according to the PDOs with CRC26 (primary tumor) and CRC26LM (liver metastasis) being closest (Supplementary Figure 4A). We identified 8 clusters (Figure 5A) which were annotated using curated panels of genes (Figure 5B, Supplementary Figure 2B-C). All PDOs included moderately differentiated stem-like cells, transient-amplifying-(TA)-like cells, goblet-like cells and M-like cells according to the respective markers (Figure 5C, Supplementary Figure 2B-C). The PDOs were highly heterogeneous with respect to the fractions of different cell types, with TA-like cells being most and M-like cells being least abundant (Figure 5C). Analyses of RNA velocity indicated cell hierarchies

according to the cancer stem cell hypothesis, with stem cells at the apex, giving rise to TA progenitor cells that undergo differentiation into several cell lineages (Figure 5A). Using a compendium of pathway-responsive gene sets we then assigned activities of 14 canonical cancer pathways to the individual cell types. The cancer pathway activities were variable between the secretory cells and other cell types, and between the PDOs (Figure 5D).

Kinase inhibitors modulate stemness and differentiation pathways

The phenotypic and differentiation plasticity of the tumor cells shown here can have profound effects on the tumor formation, malignant progression, and response to therapy. For example, it has been shown that MEK inhibitors activate *WNT* signaling and induce stem cell plasticity in CRC [61]. Similarly, an experimental evidence was provided showing that therapies targeting the MAPK pathway can redirect developmental trajectories of CRC and can be associated with therapy resistance [62]. However, both studies focused on the inhibitors targeting kinases within the canonical MAPK pathway, i.e. MEK and EGFR/BRAF/MEK. Given the extensive pathway crosstalk in our PDOs, we asked what is the effect of other inhibitors on the phenotypic and differentiation plasticity. We therefore carried out experiments and treated the PDOs for 72 hours with the used kinase inhibitors (BRAFi, MEKi, mTORi, PI3Ki, TAKi, TBKi), and analyzed markers for stemness and differentiation. The results show heterogeneous effects of the MEKi and BRAFi confirming previous studies [61,62]. Moreover, these effects were also observable for other inhibitors including mTORi, PI3Ki, TBKi, and TAKi (Figure 5E). For example in CRC02 MEKi induced upregulation of the stemness marker *LGR5* (Figure 5F), whereas in CRC26 mTORi induced both, upregulation of *LGR5* and the differentiation marker *MUC2* (Figure 5G). Similar diversity was observed for other kinase inhibitors (Figure 5F-G) and other PDOs (Supplementary Figure 2E-H).

Quantifying heterocellular signaling crosstalk using spatial single-cell proteomics profiling of tumors

Several PDOs showed upregulation of immune pathways following treatment with specific kinase inhibitors, suggesting possible synergistic effects of kinase inhibitors with immune checkpoint blockers. An effective antitumor response following combination therapy of kinase inhibitors and anti-PD-1 or anti-PD-L1 antibodies requires both the presence of CD8+ T cells in the TME as well as CD8+T cell-tumor cell interactions. We therefore used IMC-based multidimensional imaging of the tumor samples to quantify the densities of immune cell subpopulations and identify heterocellular interactions. We previously developed and evaluated a panel of antibodies for IMC (Table S2) on formalin-fixed, paraffin embedded (FFPE) samples for a comprehensive overview of the TME and cancer-immune cell interactions [43], including lineage and functional immune cell markers, surrogates of cancer cell states (proliferation, apoptosis) and structural markers (epithelium, stroma, vessels) (Supplementary Figure 5A). We used this panel and FFPE samples from five primary tumors and one liver

metastasis of the CRC patients. Following data-driven identification of single-cell phenotypes (Supplementary Figure 5B), segmentation, and image analysis, we identified 197,454 cells and quantified the densities of five major classes: myeloid, lymphoid, epithelial, fibroblasts, and endothelial cells, which could be further granulated into 41 different cell types (Figure 6A). The cell densities were highly heterogeneous, with $CD8^+$ T cells being the most abundant in MSI CRC (Figure 6B, Supplementary Figure 6A). The analyses of the co-expression of immunomodulatory molecules *PD-1*, *PD-L1*, *ICOS*, *LAG3*, *TIM3*, and *IDO* showed heterogeneous populations of immune and tumor cells (Supplementary Figure 6B). The densities of *PD-1+* immune cells and *PD-L1+* tumor cells were highest in tumors from patients CRC03 and CRC13 (Figure 6C), suggesting that these patients are candidates for immunotherapy with anti-PD1/antiPD-L1 antibodies.

In order to generate higher-order information beyond cell densities, we investigated spatial cell-cell interactions. We applied cell neighborhood analysis by defining cell nuclei and associating polygons (Voronoi diagram) to each nucleus (Figure 6D), thereby allowing cells of different sizes and distances to be assessed as neighbors [63]. We used a permutation approach to identify pairwise interactions between cell phenotypes that occurred more or less frequently than expected by chance. This spatial information revealed a number of significant cell-cell interactions, with cell pairs being close neighbors (cell-cell attraction) (Supplementary Figure 6C) or distant neighbors (cell-cell avoidance) (Supplementary Figure 6D). Cellular attractions across all tumors were detectable within the lineages of myeloid, lymphoid, epithelial, fibroblasts, and endothelial cells as well as within the classes (Supplementary Figure 6C). Importantly, neighborhood analysis of *PD-L1+*cells and *PD1+* cells (defined as direct neighborhood of at least one *PD-L1+* tumor cell with at least one *PD1+* immune cell), showed that in patient CRC13 there were *PD-L1+* tumor cells / *PD-1+* immune cells interactions whereas in patient CRC03, despite the relatively high densities of both *PD-L1+* tumor cells and *PD-1+* immune cells, there were no significant cell-cell interactions (Figure 6C-E, Table S3). Hence, based on the spatial interaction analysis only patient CRC13 would be amenable for a therapy with anti-PD1 or anti-PD-L1 antibodies.

Discussion

We developed a functional precision oncology approach using PDOs and quantitative phosphoproteomic profiling, and applied this method to demonstrate the feasibility of dissecting tumor cell signaling in individual CRC patients. The information content that can be extracted from these datasets is superior compared to the information content obtained using alternative approaches. Static (i.e. unperturbed) approaches using biopsies or surgical specimens coupled with phosphoproteomic analysis of tumor tissues [64,65] resemble the assessment of the steady-state of the phosphoproteome and are of limited value for inferring kinase signaling networks. Previous functional approaches using phosphoproteomic measurements to construct cancer signaling networks employed cell lines [15,66] and were based on mathematical models that are inherently limited to a small number of molecular interactions [15]. Recently developed platform using *ex vivo* tumor fragments [67] could be a viable alternative to the PDOs, however, given the limited amount of material that can be obtained, the phoshpoproteome coverage is substantially reduced and the number of possible drugs that can be tested highly restricted. Hence, the "next-generation" functional tests shown here enable comprehensive investigation of the intrinsic CRC biology for successfully personalizing treatment.

The results of our functional precision profiling provide new biological insights and have important translational relevance. First, and most importantly, we show that the patient-specific rewiring of the kinase signaling network is unaffected by mutations in CRC. Our results suggest that the responses to targeted therapy are determined by non-genetic mechanisms such as those conveyed by phenotypic plasticity [68]. Single-cell RNA sequencing of the PDOs showed heterogeneous pathway activation in epithelial cell subsets, further supporting the notion of non-genetic mechanisms determining cellular response to drug treatment. We also provide experimental evidence that kinase inhibitors targeting canonical and non-canonical pathways modulate stemness and differentiation pathways, implicating that also re-purposed drugs are re-routing developmental trajectories of CRC. Our finding of mutation-independent signaling rewiring is supported by a growing body of literature suggesting that cancer phenotypes and the responses to therapy are determined by non-genetic mechanisms, in addition to the mutation-driven mechanisms commonly considered. For example, a CRC classification system previously proposed associates epithelial cellular phenotypes like stem-like, Goblet-like or enterocyte cells with responses to cetuximab and standard-of-care chemotherapy [69]. Similarly, recent work using PDX models showed that EGFR inhibition in CRC tumors induces Paneth-like phenotypic rewiring [70], suggesting that cellular plasticity is shaping drug response in cancer. Hence, *in vivo* data using preclinical models and clinical data from large cohorts provide additional evidence for the importance of CRC tumor cell plasticity for the response to targeted therapy. In fact, phenotypic plasticity and disrupted differentiation have been recently proposed as discrete hallmark capability of cancer [68].

Second, we show that kinase inhibitors can induce profound off-target effects resulting in the modulation of both, oncogenic and immune-related pathways. These off-target effects might explain lack of efficacy of targeted therapies as well as failure of combination therapies with immune checkpoint blockers. Off-target effects due to signaling crosstalk, feedback and feedforward mechanisms, as well as signaling network adaptations, have been previously reported in a variety of cancers and model systems [55]. However, predicting such off-target effects of specific kinase inhibitors for individual patients based on static multi-omic measurements is not possible. Hence, information-reach assays based on perturbation experiments and phosphoproteomic measurements as presented here are required.

Third, complementing our functional precision profiling with extrinsic information from histology using IMC of the primary tumors enabled us to quantify spatial heterocellular crosstalk and tumor-immune cell interactions, and hence, provide rationale for combination therapy with immune checkpoint blockers. Thus, our *tour de force* work based on functional precision profiling and single-cell spatial analysis might serve as a blueprint for developing next-generation functional precision oncology platforms for predicting combination therapy response in individuals with metastatic CRC and possibly also other cancers.

Our work has several limitations that can be addressed in future studies. One limitation of our method for inferring kinase network topologies is the use of literature-mined networks. Literature-mined networks are biased towards well-known kinases and pathways as evident by the number of kinases used in our downstream analyses. Given the limited annotations in the public repositories we were able to use about 10% of the phosphoproteomic data (600 phosphopeptides out of 6000 measured). A promising method for revealing new information on kinase-kinase relationships based on chemical phosphoproteomics was recently published [56] and can be used to infer additional kinase-kinase interactions. Another limitation of our study is the small number of patients and PDOs. Large-scale efforts are needed to investigate big cohorts of patients and potentially identify patterns for patient stratification. Global analysis of the phosphoproteomic data here showed clustering according to patients rather than treatments. Hence, it is intriguing to speculate that there is a limited number of signaling states that could be consequently exploited to stratify patients and ultimately inform therapy. Finally, we used only bulk phosphoproteomic data and could not assign signaling pathways/states to specific epithelial cell subsets. However, technological developments using ultra-high sensitive mass spectrometers are improving [71] and could in near future enable single-cell proteome measurements to gain insights into the cellular heterogeneity.

In summary, the conceptual advances and the insights from the deep molecular and cellular phenotyping we show here challenge the notion that the information flow following kinase inhibition occurs

only within specific signaling cascades. We also provide a unique resource of high quality multi-omics and multi-modal data as well as the corresponding living biobank that can be exploited for both, investigation of intrinsic biology of CRC cells as well as the development of novel methods for interrogating intra- and inter-cellular crosstalk. Finally, our multi-modal profiling approach could provide the basis for the development of a platform for informing precision (immuno)oncology in CRC.

Data and code availability

The processed data supporting the findings of this study (including exome sequencing, RNA-sequencing, proteomics, phosphoproteomics, single-cell RNA-sequencing, high-dimensional TIFF images, single-cell spatial information and phenotypes) are available online at Zenodo (https://doi.org/10.5281/zenodo.7015015).

The MS data which were used to generate the SWATH spectral library, the SWATH raw files and the quantitative results from the SWATH-MS analysis reported in this paper have been deposited in the PRIDE proteomics data repository (https://www.ebi.ac.uk/pride/archive/) under the following accession numbers:

1) Baseline expression experiment: PXD019124;
2) Total cell lysate in cancer vs metastasis: PXD018922;
3) Perturbation expression experiment: PXD018913;
4) Spectral library for phosphopeptides: PXD018862;
5) Spectral library for total cell lysate: PXD018835:

The code used to produce the results of this study is available at https://github.com/icbi-lab/plattner_2022

Acknowledgments

This work was supported by the European Research Council (grant agreement No 786295 to ZT), by the Horizon 2020 IMI project imSAVAR (grant agreement no 853988 to ZT), by the Austrian Science Fund (FWF) (projects I3291 and I3978 to ZT, and project T974-B30 to FF), by the Vienna Science and Technology Fund (Project LS16-025 to ZT), Österreichische Krebshilfe Tirol (project FF18015 to GL). CP and GS were supported by a DOC-fellowship from the Austrian Academy of Sciences. ZT is a member of the German Research Foundation (DFG) project TRR 241(INF). Antibodies for the Western blots were kindly provided by Jakob Troppmair. We are thankful to Filipp Sokolovski for collecting clinical data.

Author contributions

ZT conceived the project. GL, RL, AN, SD, NN, NB performed the PDO experiments. CP and AK analyzed the proteomics and phosphoproteomics data. PB and AS carried out proteomics and phosphoproteomics experiments. SS and DÖ recruited patients and performed surgeries. HC, HF, and GH advised the establishment of the living biobank. AN and DW made the PDO stainings. MI performed imaging CyTOF and data analysis. DR and ZL analyzed the imaging CyTOF data. GS analyzed the transriptomics data. DR, GF, and FF analyzed the exome sequencing data and predicted the neoantigens. Anne K prepared sequencing libraries. HF, FG, LAH, RA, NFCCM, and ZT supervised the work. ZT wrote the manuscript with the input from all authors. GL, CP, PB, and AK contributed equally to this work.

Competing interests

Authors declare no competing interests.

Figure Legends

Figure 1. Schematic outline of the overall concept used in this study. Multimodal profiling of tumor specimens and PDOs in a cohort of CRC patients.

Figure 2. Proteogenomic analysis of PDOs from CRC patients. (A) Genetic profiles of the PDOs ordered according to the mutational load (ML). MMR: mismatch-repair. ML: mutational load. CNV: copy number variation. **(B)** Analysis of the cancer pathways of the PDOs using bulk RNA-seq data and PROGENy. The pathway activity scores are z-scaled and clustered hierarchically by euclidean distance and complete linkage. **(C)** Pathway analysis of the hallmark gene sets from MSigDB of the PDOs using proteomic data (SWATH-MS). The heat map shows z-scores of enrichment scores derived from Gene Set Variation Analysis (GSVA) and clustered hierarchically by Pearson correlation as distance metric and complete linkage. **(D)** Correlation analysis between RNA-seq data and proteomics data. The histogram shows gene-wise Pearson correlation between transcriptome and proteome levels. Denoted are driver genes (black) and immune-related genes (red). The average gene-wise Pearson correlation is 0.29 (dashed line). **(E)** Protein complexes ranked according to the co-abundance observed for complex members. Shaded areas, left: stable complexes (top 25%), right: variable complexes (bottom 25%). MCM: mini chromosome maintenance. COP9: constitutive photomorphogenesis 9. **(F)** Variance of the protein levels of the 26S proteasome subunits across all PDOs.

Figure 3. Functional profiling experiments of the PDOs with targeted drugs. (A) PCA of the phosphoproteomic data. **(B)** UpSet plot of regulated phosphopeptides (|log2FC|>1, FDR<0.05) following treatment with specific kinase inhibitors. **(C)** Heatmap of normalized enrichment scores (NES) of phosphorylation signatures from PTMSigDB [41] and SIGNOR [40] with at least five phosphorylation sites representing changes in kinase activities following treatment of PDOs with specific kinase inhibitors or TNFα (FDR<0.05), clustered by complete linkage of Euclidean distances. **(D)** Normalized enrichment scores (NES) of phosphorylation signatures representing changes in pathway activities following treatment of PDOs with specific kinase inhibitors or TNFα (FDR<0.05, database and number of phosphorylation sites shown in brackets).

Figure 4. Comparative analysis of the kinase network topologies for the perturbed PDOs. (A) Visual representation of the reconstructed kinase networks. Highlighted in blue are kinases harboring mutations. **(B)** Betweenness and degree centrality measures of kinase nodes in the networks shown in **(A)**.

Figure 5. Single cell analysis of PDOs from CRC patients. (A) UMAP plot of batch-corrected scRNA-seq dataset from all organoids, colored by cell-type. RNA velocity vectors are projected on top of the UMAP plot. **(B)** UMAP plot from (A) colored by gene expression (log(CPM)) of the markers for stem cells (*LGR5*), Wnt target (*AXIN2*), goblet cells (TFF3), and enterocytes (*FABP1*). **(C)** Cellular composition of the PDOs as measured by scRNA-seq. **(D)** Analysis of cancer pathways activation in specific epithelial cell types using PROGENy [23]. **(E)** Heat map of regulation of stem cell markers and differentiation markers following treatments with different kinase inhibitors for 72 hours and qPCR measurements. Each drug treatment was performed in triplicates. Fold change in expression of target genes was calculated by $2^{-\Delta\Delta CT}$ method [72] using DMSO control for normalization, and GAPDH as an endogenous control. * $p < 0.01$; unpaired two-tailed Student's t-test. **(F-G)** Relative mRNA expression of CRC02 and CRC26 organoids from the analysis shown in (E). Error bars indicate + SD and p-values show significant differences between the treated vs DMSO control.* $p < 0.05$, ** $p < 0.01$, *** $p < 0.001$, unpaired two-tailed Student's t-test.

Fig. 6 Spatial proteomics of tumor samples using imaging mass cytometry. (A) Cellular composition of the TME using 41 cell phenotypes from six tumor tissues from the respective patients. **(B)** Cell densities of $CD8^+$, $CD4^+$, $CD45RO^+$ and Tregs. **(C)** Cell densities of $PD1^+$ tumor cells and $PD\text{-}L1^+$ immune cells. **(D)** Example subsection (200x200 µm) of cell neighborhood analysis using Voronoi diagrams. Upper panel: original image. Lower panel: map following cell phenotype identification and building of Voronoi diagrams. **(E)** Example subsection (200x200 µm) of the cell neighborhood analysis for $PD1^+$ tumor cells and $PD\text{-}L1^+$ immune cells interactions in CRC 13 (left) and CRC03 (right).

Supplementary Figure Legends

Supplementary Figure 1. Genomic and transcriptomic characterisation of PDOs. (**A)** IF staining of tumor PDOs with Lysozyme (Paneth cells), Chromogranin A (Chr-A) (Enteroendocrine cells), Ki-67 (proliferating cells), MUC2 (Mucin 2) (Goblet cells), EpCAM (arrows point to EpCAM expression, epithelial cells), Phalloidin (F-actin) (brush border), SOX9 and Lgr5+ for (stem cells), and Hoechst (DNA). (Scale bars: 50 µm.). **(B)** Copy number variation analysis for PDOs. Red: amplifications. Blue: deletions. **(C)** Heat map of the steady-state RNA-sequencing data. Eight major clusters were defined and annotated using GO enrichment analysis. The genes are z-scaled and clustered hierarchically by using Pearson correlation as distance and complete linkage. (**D**) Heat map of immune-related genes grouped as antigen presenting cell receptors (APCr), chemokines, chemokine receptors, cytokines, human leukocyte antigens (HLA) and interferon gamma (IFNg). ISG.RS: interferon metagene for IFNG signature genes [73] . (**E**) Heat map of the steady-state proteomics data. Eight major clusters were defined and presented the same way as the gene expressions in (C). (**F**) Heat map representing z-scores of the log2-transformed protein levels of the subunits of the immunoproteasome.

Supplementary Figure 2. **Analysis of the phosphoproteomic data following signaling perturbations.** (**A**) Western blots for selected targets of kinase inhibitors. (**B**) Log-2-fold-changes in the phosphorylation of residues selected as potential downstream targets of kinase inhibitors/activators following the respective treatments (FDR<0.05). (**C**) Heatmap of all log-2-fold-changes in the phosphorylation of residues with FDR<0.05 in at least one treatment, clustered by complete linkage of Euclidean distances.. (**D**) Volcano plots of normalized enrichment scores (NES) for kinase activity signatures from PTMSigDB [41] and SIGNOR [40] following treatment of PDOs with specific kinase inhibitors or TNFα.

Supplementary Figure 3. **Signaling networks**. (**A**) Kinase signaling networks for specific PDOs constructed using the phosphoproteomic perturbation data (related to Figure 4A). Log-2-fold changes in kinase activities of significantly perturbed nodes are shown for each treatment.

Supplementary Figure 4. **Single-cell RNA-seq analysis of the PDOs.** (**A**) UMAP of the scRNA-seq data, colored by PDO. (**B**) Violin plots for selected markers. (**C**) Dot plots for the markers used for cell annotation. (D) UMAP of the RNA-sequencing data, colored by cell type. (E-H) Regulation of stem cell markers and differentiation markers following treatments with different kinase inhibitors and qPCR measurements for CRC03, CRC04, CRC13 and CRC26. Each drug treatment was performed in triplicates. Error bars indicate + SD and p-values show significant differences between the treated vs DMSO control.* $p < 0.05$, ** $p < 0.01$, *** $p < 0.001$, unpaired two-tailed Student's t-test.

Supplementary Figure 5. **Preprocessing of the imaging mass cytometry data**. (**A**) Example IMC images of the major cell types (pseudo coloured) for selected organoids, showing their heterogeneity. Subgroups of major cell types are coloured in similar colour shades. (**B**) Hierarchical clustering of the measured expression values of 34 selected markers used for the phenotyping and recognition of different cell types.

Supplementary Figure 6. **Imaging mass cytometry analyses of the tumors**. (**A**) Cell densities for the four major cell types. (**B**) Cell densities for selected immuno-modulatory molecules. (**C**) Interaction analysis showing cell-cell attraction. Squares are showing the number of PDOs in which significant interactions occur. (**D**) Interaction analysis showing cell-cell avoidance. Squares are showing the number of PDOs in which significant interactions occur.

REFERENCES

1. H. Sung, Global Cancer Statistics 2020: GLOBOCAN Estimates of Incidence and Mortality Worldwide for 36 Cancers in 185 Countries, CA Cancer J Clin. 71 (2021) 209-249,. https://doi.org/10.3322/caac.21660.
2. F. Nicolantonio, Precision oncology in metastatic colorectal cancer - from biology to medicine, Nat. Rev. Clin. Oncol. 18 (2021) 506-525,. https://doi.org/10.1038/s41571-021-00495-z.
3. Cancer Genome Atlas, N. Comprehensive molecular characterization of human colon and rectal cancer, Nature. 487 (2012) 330-337,. https://doi.org/10.1038/nature11252.
4. D.T. Le, PD-1 Blockade in Tumors with Mismatch-Repair Deficiency, N. Engl. J. Med. 372 (2015) 2509-2520,. https://doi.org/10.1056/NEJMoa1500596.
5. J. Galon, Type, density, and location of immune cells within human colorectal tumors predict clinical outcome, Science. 313 (2006) 1960-1964,. https://doi.org/10.1126/science.1129139.
6. A. Letai, P. Bhola, A.L. Welm, Functional precision oncology: Testing tumors with drugs to identify vulnerabilities and novel combinations, Cancer Cell. 40 (2022) 26-35,. https://doi.org/10.1016/j.ccell.2021.12.004.
7. J. Drost, H. Clevers, Organoids in cancer research, Nat. Rev. Cancer. 18 (2018) 407-418,. https://doi.org/10.1038/s41568-018-0007-6.
8. G. Vlachogiannis, Patient-derived organoids model treatment response of metastatic gastrointestinal cancers, Science. 359 (2018) 920-926,. https://doi.org/10.1126/science.aao2774.
9. S.N. Ooft, Patient-derived organoids can predict response to chemotherapy in metastatic colorectal cancer patients, Sci. Transl. Med. 11 (2019). https://doi.org/10.1126/scitranslmed.aay2574.
10. G.E. Wensink, Patient-derived organoids as a predictive biomarker for treatment response in cancer patients, NPJ Precis Oncol. 5, 30 (2021). https://doi.org/10.1038/s41698-021-00168-1.
11. S.N. Ooft, Prospective experimental treatment of colorectal cancer patients based on organoid drug responses, ESMO Open. 6, 100103 (2021). https://doi.org/10.1016/j.esmoop.2021.100103.
12. M.B. Yaffe, Why geneticists stole cancer research even though cancer is primarily a signaling disease, Sci Signal. 12 (2019). https://doi.org/10.1126/scisignal.aaw3483.
13. L.C. Gillet, Targeted data extraction of the MS/MS spectra generated by data-independent acquisition: a new concept for consistent and accurate proteome analysis, Mol Cell Proteomics. 11, O111 016717 (2012). https://doi.org/10.1074/mcp.O111.016717.
14. C. Ludwig, Data-independent acquisition-based SWATH-MS for quantitative proteomics: a tutorial, Mol Syst Biol. 14, e8126 (2018). https://doi.org/10.15252/msb.20178126.
15. F. Eduati, Drug Resistance Mechanisms in Colorectal Cancer Dissected with Cell Type-Specific Dynamic Logic Models, Cancer Res. 77 (2017) 3364-3375,. https://doi.org/10.1158/0008-5472.CAN-17-0078.
16. J.N. Buzzelli, D. Ouaret, G. Brown, P.D. Allen, R.J. Muschel, Colorectal cancer liver metastases organoids retain characteristics of original tumor and acquire chemotherapy resistance, Stem Cell Res. 27 (2018) 109–120. https://doi.org/10.1016/j.scr.2018.01.016.
17. G. Rosenberger, C.C. Koh, T. Guo, H.L. Röst, P. Kouvonen, B.C. Collins, M. Heusel, Y. Liu, E. Caron, A. Vichalkovski, M. Faini, O.T. Schubert, P. Faridi, H.A. Ebhardt, M. Matondo, H. Lam, S.L. Bader, D.S. Campbell, E.W. Deutsch, R.L. Moritz, S. Tate, R. Aebersold, A repository of assays to quantify 10,000 human proteins by SWATH-MS, Sci. Data. 1 (2014) 140031. https://doi.org/10.1038/sdata.2014.31.
18. D. Rieder, G. Fotakis, M. Ausserhofer, G. René, W. Paster, Z. Trajanoski, F. Finotello, nextNEOpi: a comprehensive pipeline for computational neoantigen prediction, Bioinforma. Oxf. Engl. (2021) btab759. https://doi.org/10.1093/bioinformatics/btab759.

19. B. Niu, K. Ye, Q. Zhang, C. Lu, M. Xie, M.D. McLellan, M.C. Wendl, L. Ding, MSIsensor: microsatellite instability detection using paired tumor-normal sequence data, Bioinforma. Oxf. Engl. 30 (2014) 1015–1016. https://doi.org/10.1093/bioinformatics/btt755.

20. P.A. Ewels, A. Peltzer, S. Fillinger, H. Patel, J. Alneberg, A. Wilm, M.U. Garcia, P. Di Tommaso, S. Nahnsen, The nf-core framework for community-curated bioinformatics pipelines, Nat. Biotechnol. 38 (2020) 276–278. https://doi.org/10.1038/s41587-020-0439-x.

21. A. Dobin, C.A. Davis, F. Schlesinger, J. Drenkow, C. Zaleski, S. Jha, P. Batut, M. Chaisson, T.R. Gingeras, STAR: ultrafast universal RNA-seq aligner, Bioinforma. Oxf. Engl. 29 (2013) 15–21. https://doi.org/10.1093/bioinformatics/bts635.

22. B. Li, C.N. Dewey, RSEM: accurate transcript quantification from RNA-Seq data with or without a reference genome, BMC Bioinformatics. 12 (2011) 323. https://doi.org/10.1186/1471-2105-12-323.

23. M. Schubert, Perturbation-response genes reveal signaling footprints in cancer gene expression, Nat Commun. 9, 20 (2018). https://doi.org/10.1038/s41467-017-02391-6.

24. G. Yu, L.-G. Wang, Y. Han, Q.-Y. He, clusterProfiler: an R package for comparing biological themes among gene clusters, Omics J. Integr. Biol. 16 (2012) 284–287. https://doi.org/10.1089/omi.2011.0118.

25. Z. Gu, R. Eils, M. Schlesner, Complex heatmaps reveal patterns and correlations in multidimensional genomic data, Bioinforma. Oxf. Engl. 32 (2016) 2847–2849. https://doi.org/10.1093/bioinformatics/btw313.

26. F.A. Wolf, P. Angerer, F.J. Theis, SCANPY: large-scale single-cell gene expression data analysis, Genome Biol. 19 (2018) 15. https://doi.org/10.1186/s13059-017-1382-0.

27. N.J. Bernstein, N.L. Fong, I. Lam, M.A. Roy, D.G. Hendrickson, D.R. Kelley, Solo: Doublet Identification in Single-Cell RNA-Seq via Semi-Supervised Deep Learning, Cell Syst. 11 (2020) 95-101.e5. https://doi.org/10.1016/j.cels.2020.05.010.

28. R. Lopez, A. Gayoso, N. Yosef, Enhancing scientific discoveries in molecular biology with deep generative models, Mol. Syst. Biol. 16 (2020) e9198. https://doi.org/10.15252/msb.20199198.

29. E. Becht, L. McInnes, J. Healy, C.-A. Dutertre, I.W.H. Kwok, L.G. Ng, F. Ginhoux, E.W. Newell, Dimensionality reduction for visualizing single-cell data using UMAP, Nat. Biotechnol. (2018). https://doi.org/10.1038/nbt.4314.

30. V.A. Traag, L. Waltman, N.J. van Eck, From Louvain to Leiden: guaranteeing well-connected communities, Sci. Rep. 9 (2019) 5233. https://doi.org/10.1038/s41598-019-41695-z.

31. R. Lopez, J. Regier, M.B. Cole, M.I. Jordan, N. Yosef, Deep generative modeling for single-cell transcriptomics, Nat. Methods. 15 (2018) 1053–1058. https://doi.org/10.1038/s41592-018-0229-2.

32. G. La Manno, R. Soldatov, A. Zeisel, E. Braun, H. Hochgerner, V. Petukhov, K. Lidschreiber, M.E. Kastriti, P. Lönnerberg, A. Furlan, J. Fan, L.E. Borm, Z. Liu, D. van Bruggen, J. Guo, X. He, R. Barker, E. Sundström, G. Castelo-Branco, P. Cramer, I. Adameyko, S. Linnarsson, P.V. Kharchenko, RNA velocity of single cells, Nature. 560 (2018) 494–498. https://doi.org/10.1038/s41586-018-0414-6.

33. V. Bergen, M. Lange, S. Peidli, F.A. Wolf, F.J. Theis, Generalizing RNA velocity to transient cell states through dynamical modeling, Nat. Biotechnol. 38 (2020) 1408–1414. https://doi.org/10.1038/s41587-020-0591-3.

34. C.H. Holland, J. Tanevski, J. Perales-Patón, J. Gleixner, M.P. Kumar, E. Mereu, B.A. Joughin, O. Stegle, D.A. Lauffenburger, H. Heyn, B. Szalai, J. Saez-Rodriguez, Robustness and applicability of transcription factor and pathway analysis tools on single-cell RNA-seq data, Genome Biol. 21 (2020) 36. https://doi.org/10.1186/s13059-020-1949-z.

35. G. Teo, S. Kim, C.-C. Tsou, B. Collins, A.-C. Gingras, A.I. Nesvizhskii, H. Choi, mapDIA: Preprocessing and statistical analysis of quantitative proteomics data from data independent acquisition mass spectrometry, J. Proteomics. 129 (2015) 108–120. https://doi.org/10.1016/j.jprot.2015.09.013.

36. S. Hänzelmann, R. Castelo, J. Guinney, GSVA: gene set variation analysis for microarray and RNA-seq data, BMC Bioinformatics. 14 (2013) 7. https://doi.org/10.1186/1471-2105-14-7.

37. A. Liberzon, C. Birger, H. Thorvaldsdóttir, M. Ghandi, J.P. Mesirov, P. Tamayo, The Molecular Signatures Database (MSigDB) hallmark gene set collection, Cell Syst. 1 (2015) 417–425. https://doi.org/10.1016/j.cels.2015.12.004.

38. A. Ori, M. Iskar, K. Buczak, P. Kastritis, L. Parca, A. Andrés-Pons, S. Singer, P. Bork, M. Beck, Spatiotemporal variation of mammalian protein complex stoichiometries, Genome Biol. 17 (2016) 47. https://doi.org/10.1186/s13059-016-0912-5.

39. UniProt Consortium, UniProt: a worldwide hub of protein knowledge, Nucleic Acids Res. 47 (2019) D506–D515. https://doi.org/10.1093/nar/gky1049.

40. L. Licata, SIGNOR 2.0, the SIGnaling Network Open Resource 2.0: 2019 update, Nucleic Acids Res. 48 (2020) 504-510,. https://doi.org/10.1093/nar/gkz949.

41. K. Krug, A Curated Resource for Phosphosite-specific Signature Analysis, Mol Cell Proteomics. 18 (2019) 576-593,. https://doi.org/10.1074/mcp.TIR118.000943.

42. G. Csárdi, T. Nepusz, The igraph software package for complex network research, Inter J. Complex Systems 1695 (2006) 1–9. https://www.semanticscholar.org/paper/The-igraph-software-package-for-complex-network-Cs%C3%A1rdi-Nepusz/1d2744b83519657f5f2610698a8ddd177ced4f5c (accessed August 5, 2022).

43. M.E. Ijsselsteijn, R. Breggen, A. Farina Sarasqueta, F. Koning, N. Miranda, A 40-Marker Panel for High Dimensional Characterization of Cancer Immune Microenvironments by Imaging Mass Cytometry, Front. Immunol. 10 (2019) 2534,. https://doi.org/10.3389/fimmu.2019.02534.

44. S. Berg, D. Kutra, T. Kroeger, C.N. Straehle, B.X. Kausler, C. Haubold, M. Schiegg, J. Ales, T. Beier, M. Rudy, K. Eren, J.I. Cervantes, B. Xu, F. Beuttenmueller, A. Wolny, C. Zhang, U. Koethe, F.A. Hamprecht, A. Kreshuk, ilastik: interactive machine learning for (bio)image analysis, Nat. Methods. 16 (2019) 1226–1232. https://doi.org/10.1038/s41592-019-0582-9.

45. A.E. Carpenter, T.R. Jones, M.R. Lamprecht, C. Clarke, I.H. Kang, O. Friman, D.A. Guertin, J.H. Chang, R.A. Lindquist, J. Moffat, P. Golland, D.M. Sabatini, CellProfiler: image analysis software for identifying and quantifying cell phenotypes, Genome Biol. 7 (2006) R100. https://doi.org/10.1186/gb-2006-7-10-r100.

46. A. Somarakis, V. Van Unen, F. Koning, B. Lelieveldt, T. Hollt, ImaCytE: Visual Exploration of Cellular Micro-Environments for Imaging Mass Cytometry Data, IEEE Trans. Vis. Comput. Graph. 27 (2021) 98–110. https://doi.org/10.1109/TVCG.2019.2931299.

47. V. van Unen, T. Höllt, N. Pezzotti, N. Li, M.J.T. Reinders, E. Eisemann, F. Koning, A. Vilanova, B.P.F. Lelieveldt, Visual analysis of mass cytometry data by hierarchical stochastic neighbour embedding reveals rare cell types, Nat. Commun. 8 (2017) 1740. https://doi.org/10.1038/s41467-017-01689-9.

48. T. Sato, Long-term expansion of epithelial organoids from human colon, adenoma, adenocarcinoma, and Barrett's epithelium, Gastroenterology. 141 (2011) 1762-1772,. https://doi.org/10.1053/j.gastro.2011.07.050.

49. F. Martinez-Jimenez, A compendium of mutational cancer driver genes, Nat. Rev. Cancer. 20 (2020) 555-572,. https://doi.org/10.1038/s41568-020-0290-x.

50. C.S. Grasso, Genetic Mechanisms of Immune Evasion in Colorectal Cancer, Cancer Discov. 8 (2018) 730-749,. https://doi.org/10.1158/2159-8290.CD-17-1327.

51. J.L. Benci, Tumor Interferon Signaling Regulates a Multigenic Resistance Program to Immune Checkpoint Blockade, Cell. 167 (2016) 1540–1554. https://doi.org/10.1016/j.cell.2016.11.022.

52. D.P. Nusinow, Quantitative Proteomics of the Cancer Cell Line Encyclopedia, Cell. 180 (2020) 387-402 316,. https://doi.org/10.1016/j.cell.2019.12.023.

53. N. Romanov, Disentangling Genetic and Environmental Effects on the Proteotypes of Individuals, Cell. 177 (2019) 1308-1318 1310,. https://doi.org/10.1016/j.cell.2019.03.015.

54. S. Kalaora, Immunoproteasome expression is associated with better prognosis and response to checkpoint therapies in melanoma, Nat Commun. 11, 896 (2020). https://doi.org/10.1038/s41467-020-14639-9.

55. W. Kolch, M. Halasz, M. Granovskaya, B.N. Kholodenko, The dynamic control of signal transduction networks in cancer cells, Nat. Rev. Cancer. 15 (2015) 515-527,. https://doi.org/10.1038/nrc3983.

56. M. Hijazi, R. Smith, V. Rajeeve, C. Bessant, P.R. Cutillas, Reconstructing kinase network topologies from phosphoproteomics data reveals cancer-associated rewiring, Nat. Biotechnol. 38 (2020) 493-502,. https://doi.org/10.1038/s41587-019-0391-9.

57. R.J. Walter, S.J. Sonnentag, V. Orian-Rousseau, L. Munoz-Sagredo, Plasticity in Colorectal Cancer: Why Cancer Cells Differentiate, Cancers Basel. 13 (2021). https://doi.org/10.3390/cancers13040918.

58. E. Batlle, H. Clevers, Cancer stem cells revisited, Nat Med. 23 (2017) 1124-1134,. https://doi.org/10.1038/nm.4409.

59. M. Fleming, S. Ravula, S.F. Tatishchev, H.L. Wang, Colorectal carcinoma: Pathologic aspects, J Gastrointest Oncol. 3 (2012) 153-173,. https://doi.org/10.3978/j.issn.2078-6891.2012.030.

60. S.A. Miller, LSD1 and Aberrant DNA Methylation Mediate Persistence of Enteroendocrine Progenitors That Support BRAF-Mutant Colorectal Cancer, Cancer Res. 81 (2021) 3791-3805,. https://doi.org/10.1158/0008-5472.CAN-20-3562.

61. T. Zhan, MEK inhibitors activate Wnt signalling and induce stem cell plasticity in colorectal cancer, Nat Commun. 10 (2019) 2197,. https://doi.org/10.1038/s41467-019-09898-0.

62. F. Uhlitz, Mitogen-activated protein kinase activity drives cell trajectories in colorectal cancer, EMBO Mol Med. 13, e14123 (2021). https://doi.org/10.15252/emmm.202114123.

63. K.S.S. Enfield, Hyperspectral cell sociology reveals spatial tumor-immune cell interactions associated with lung cancer recurrence, J Immunother Cancer. 7 (2019) 13,. https://doi.org/10.1186/s40425-018-0488-6.

64. S. Vasaikar, Proteogenomic Analysis of Human Colon Cancer Reveals New Therapeutic Opportunities, Cell. 177 (2019) 1035–1049. https://doi.org/10.1016/j.cell.2019.03.030.

65. J.M. Drake, Phosphoproteome Integration Reveals Patient-Specific Networks in Prostate Cancer, Cell. 166 (2016) 1041-1054,. https://doi.org/10.1016/j.cell.2016.07.007.

66. A. Korkut, Perturbation biology nominates upstream-downstream drug combinations in RAF inhibitor resistant melanoma cells, Elife. 4 (2015). https://doi.org/10.7554/eLife.04640.

67. P. Voabil, An ex vivo tumor fragment platform to dissect response to PD-1 blockade in cancer, Nat. Med. 27 (2021) 1250-1261,. https://doi.org/10.1038/s41591-021-01398-3.

68. D. Hanahan, Hallmarks of Cancer: New Dimensions, Cancer Discov. 12 (2022) 31-46,. https://doi.org/10.1158/2159-8290.CD-21-1059.

69. A. Sadanandam, A colorectal cancer classification system that associates cellular phenotype and responses to therapy, Nat. Med. 19 (2013) 619-625,. https://doi.org/10.1038/nm.3175.

70. B. Lupo, Colorectal cancer residual disease at maximal response to EGFR blockade displays a druggable Paneth cell-like phenotype, Sci. Transl. Med. 12 (2020). https://doi.org/10.1126/scitranslmed.aax8313.

71. A.D. Brunner, Ultra-high sensitivity mass spectrometry quantifies single-cell proteome changes upon perturbation, Mol Syst Biol. 18, e10798 (2022). https://doi.org/10.15252/msb.202110798.

72. K.J. Livak, T.D. Schmittgen, Analysis of relative gene expression data using real-time quantitative PCR and the 2(-Delta Delta C(T)) Method, Methods San Diego Calif. 25 (2001) 402–408. https://doi.org/10.1006/meth.2001.1262.

73. J.L. Benci, L.R. Johnson, R. Choa, Y. Xu, J. Qiu, Z. Zhou, B. Xu, D. Ye, K.L. Nathanson, C.H. June, E.J. Wherry, N.R. Zhang, H. Ishwaran, M.D. Hellmann, J.D. Wolchok, T. Kambayashi, A.J. Minn, Opposing Functions of Interferon Coordinate Adaptive and Innate Immune Responses to Cancer Immune Checkpoint Blockade, Cell. 178 (2019) 933-948.e14. https://doi.org/10.1016/j.cell.2019.07.019.

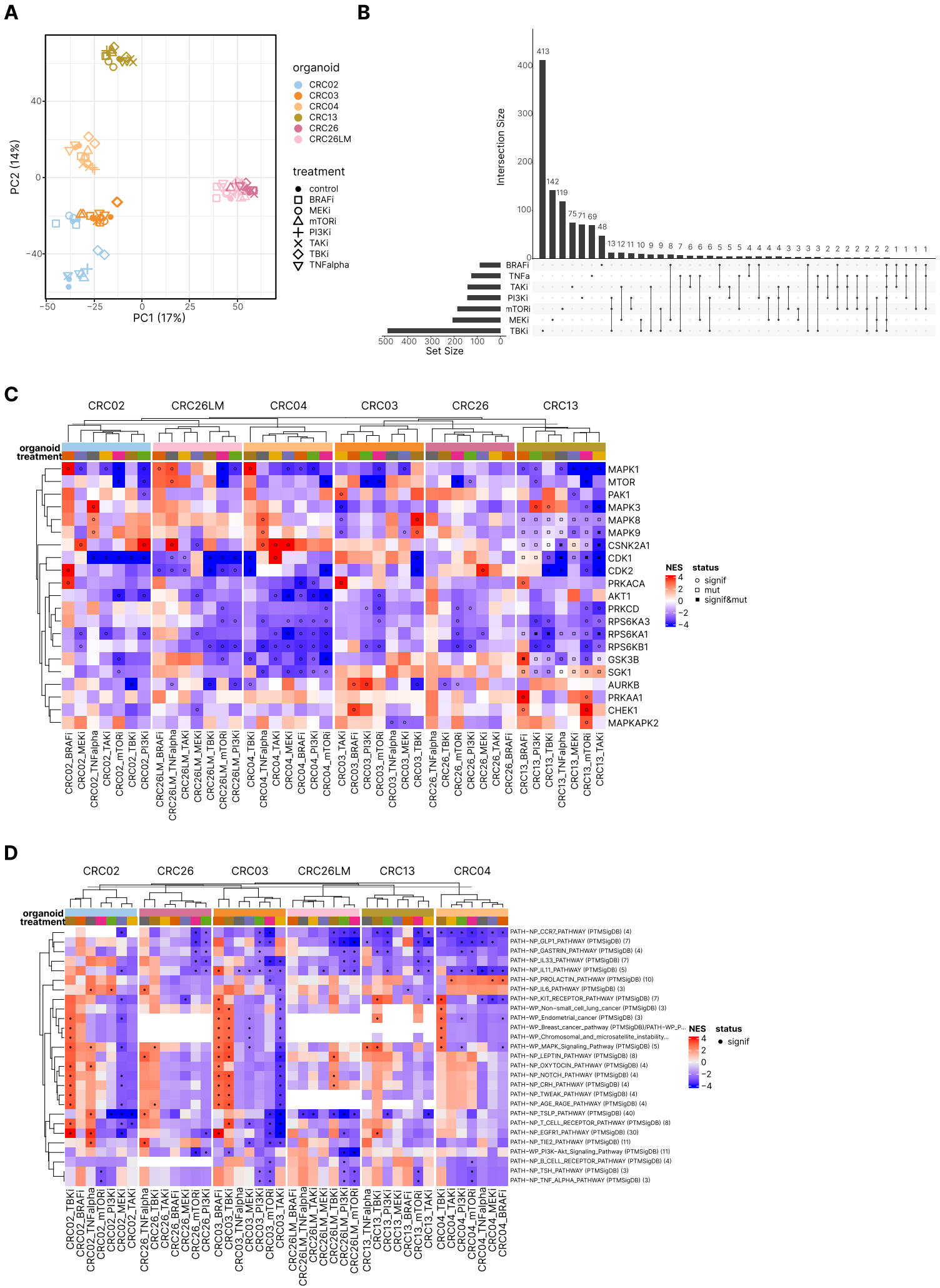
A
PC2 (14%)
PC1 (17%)
organoid
CRC02
CRC03
CRC04
CRC13
CRC26
CRC26LM
treatment
control
BRAFi
MEKi
mTORi
PI3Ki
TAKi
TBKi
TNFalpha
B
Intersection Size
Set Size
BRAFi
TNFa
TAKi
PI3Ki
mTORi
MEKi
TBKi
C
CRC02
CRC26LM
CRC04
CRC03
CRC26
CRC13
organoid
treatment
MAPK1
MTOR
PAK1
MAPK3
MAPK8
MAPK9
CSNK2A1
CDK1
CDK2
PRKACA
AKT1
PRKCD
RPS6KA3
RPS6KA1
RPS6KB1
GSK3B
SGK1
AURKB
PRKAA1
CHEK1
MAPKAPK2
NES
status
signif
mut
signif&mut
D
CRC02
CRC26
CRC03
CRC26LM
CRC13
CRC04
organoid
treatment
PATH-NP_CCR7_PATHWAY (PTMSigDB) (4)
PATH-NP_GLP1_PATHWAY (PTMSigDB) (7)
PATH-NP_GASTRIN_PATHWAY (PTMSigDB) (4)
PATH-NP_IL33_PATHWAY (PTMSigDB) (7)
PATH-NP_IL11_PATHWAY (PTMSigDB) (5)
PATH-NP_PROLACTIN_PATHWAY (PTMSigDB) (10)
PATH-NP_IL6_PATHWAY (PTMSigDB) (3)
PATH-NP_KIT_RECEPTOR_PATHWAY (PTMSigDB) (7)
PATH-WP_Non-small_cell_lung_cancer (PTMSigDB) (3)
PATH-WP_Endometrial_cancer (PTMSigDB) (3)
PATH-WP_Breast_cancer_pathway (PTMSigDB)/PATH-WP_P...
PATH-WP_Chromosomal_and_microsatellite_instability...
PATH-WP_MAPK_Signaling_Pathway (PTMSigDB) (5)
PATH-NP_LEPTIN_PATHWAY (PTMSigDB) (8)
PATH-NP_OXYTOCIN_PATHWAY (PTMSigDB) (4)
PATH-NP_NOTCH_PATHWAY (PTMSigDB) (4)
PATH-NP_CRH_PATHWAY (PTMSigDB) (4)
PATH-NP_TWEAK_PATHWAY (PTMSigDB) (4)
PATH-NP_AGE_RAGE_PATHWAY (PTMSigDB) (4)
PATH-NP_TSLP_PATHWAY (PTMSigDB) (40)
PATH-NP_T_CELL_RECEPTOR_PATHWAY (PTMSigDB) (8)
PATH-NP_EGFR1_PATHWAY (PTMSigDB) (30)
PATH-NP_TIE2_PATHWAY (PTMSigDB) (11)
PATH-WP_PI3K-Akt_Signaling_Pathway (PTMSigDB) (11)
PATH-NP_B_CELL_RECEPTOR_PATHWAY (PTMSigDB) (4)
PATH-NP_TSH_PATHWAY (PTMSigDB) (3)
PATH-NP_TNF_ALPHA_PATHWAY (PTMSigDB) (3)
NES
status
signif

Figure 3

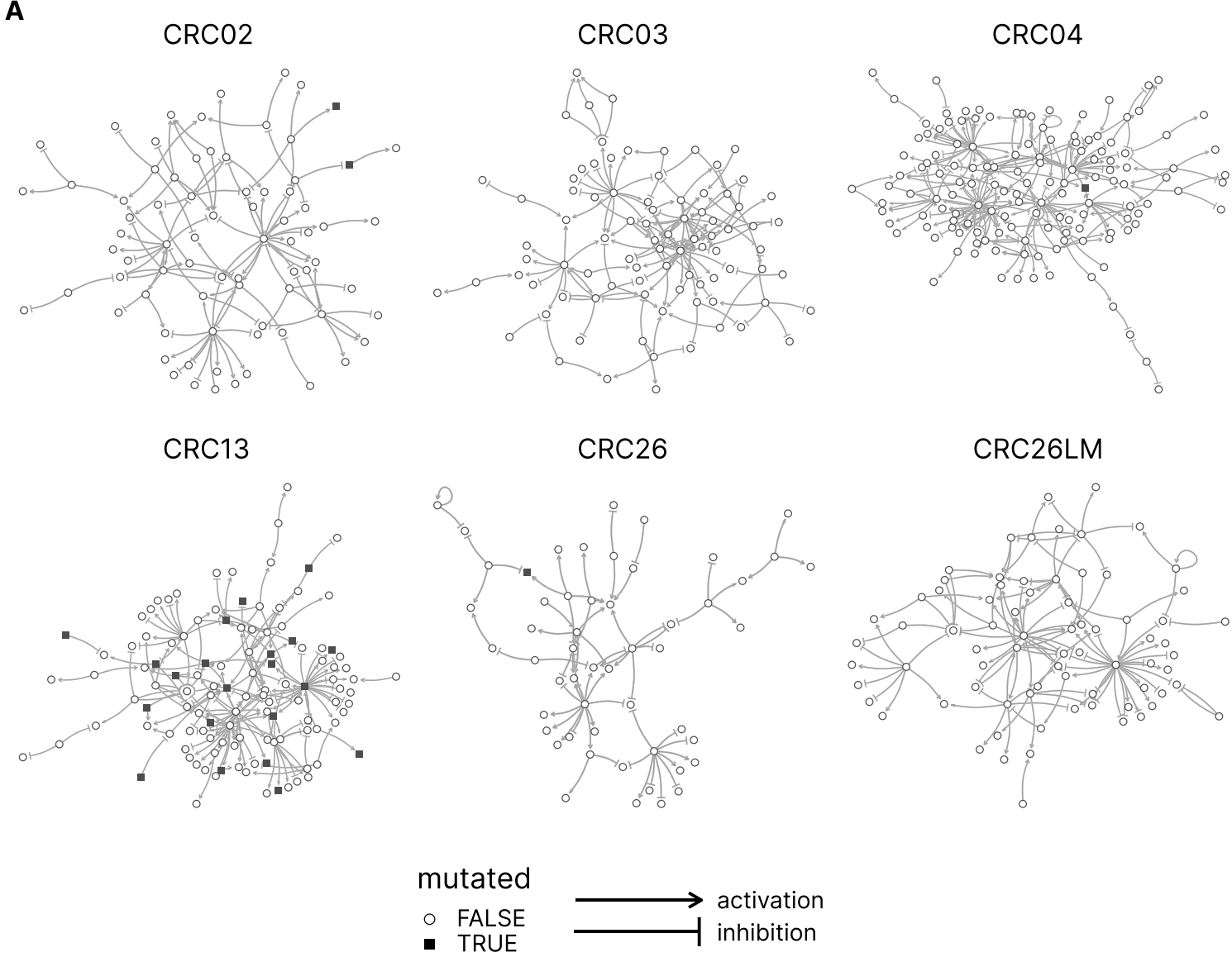
A
CRC02
CRC03
CRC04
CRC13
CRC26
CRC26LM
mutated
FALSE
TRUE
activation
inhibition

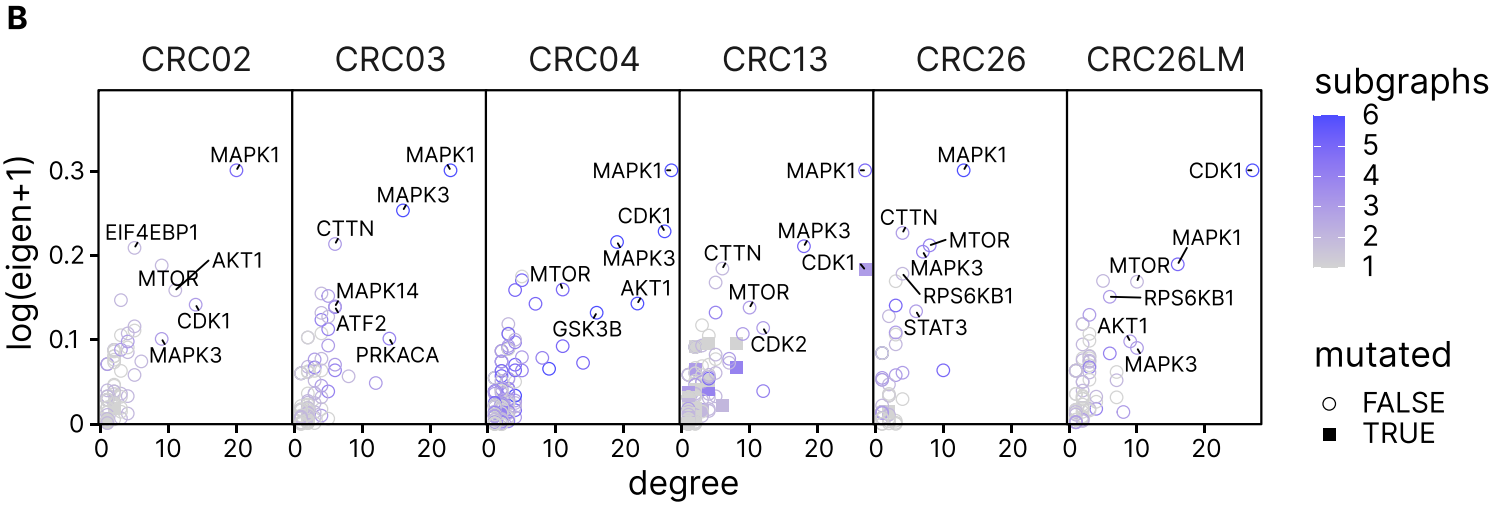
B
CRC02
CRC03
CRC04
CRC13
CRC26
CRC26LM
log(eigen+1)
degree
MAPK1
EIF4EBP1
AKT1
MTOR
CDK1
MAPK3
CTTN
MAPK14
ATF2
PRKACA
GSK3B
CDK2
RPS6KB1
STAT3
subgraphs
6
5
4
3
2
1
mutated
FALSE
TRUE

Figure 4

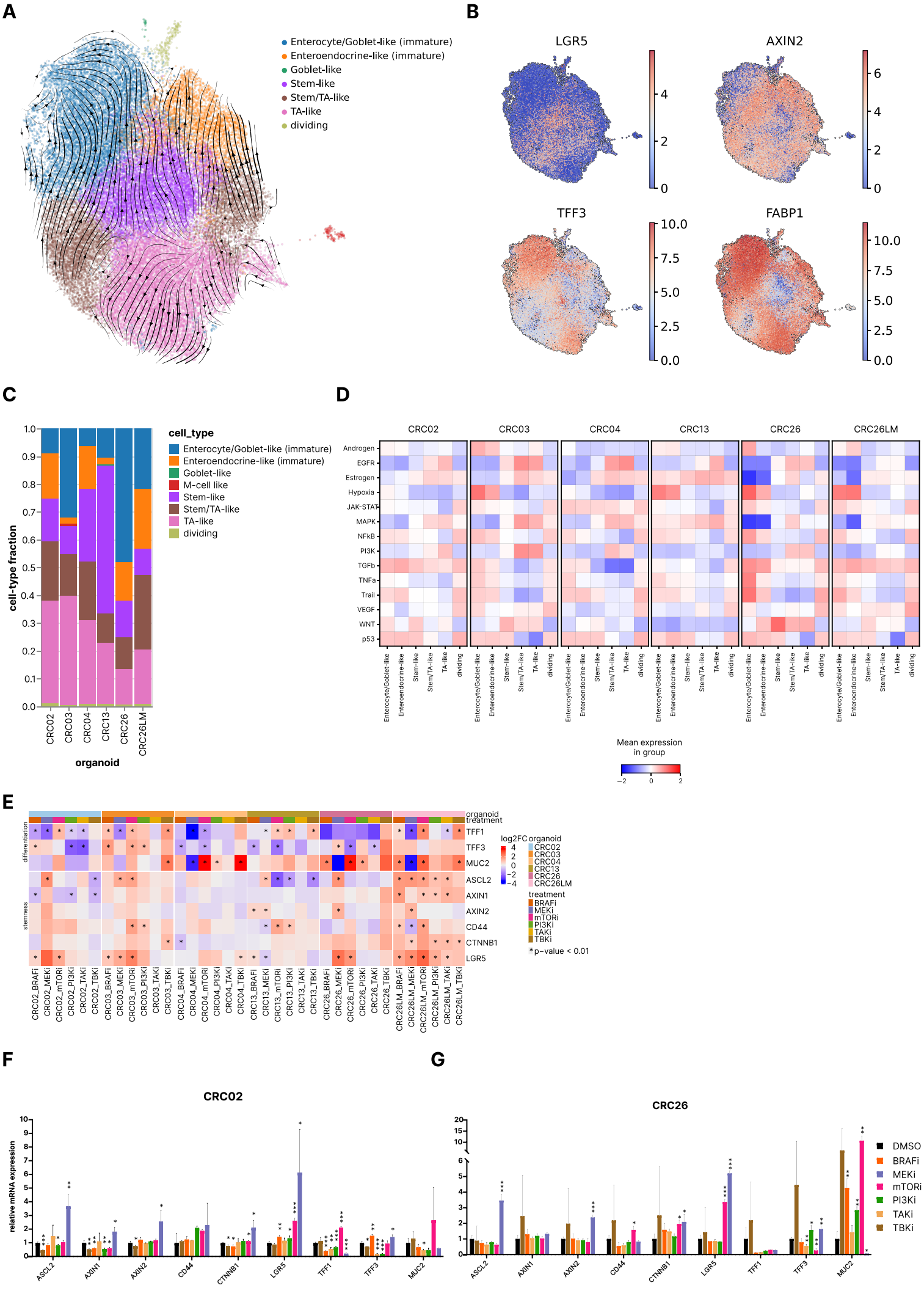
A
Enterocyte/Goblet-like (immature)
Enteroendocrine-like (immature)
Goblet-like
Stem-like
Stem/TA-like
TA-like
dividing
B
LGR5
AXIN2
TFF3
FABP1
C
cell_type
Enterocyte/Goblet-like (immature)
Enteroendocrine-like (immature)
Goblet-like
M-cell like
Stem-like
Stem/TA-like
TA-like
dividing
cell-type fraction
organoid
CRC02
CRC03
CRC04
CRC13
CRC26
CRC26LM
D
Androgen
EGFR
Estrogen
Hypoxia
JAK-STAT
MAPK
NFkB
PI3K
TGFb
TNFa
Trail
VEGF
WNT
p53
Mean expression in group
E
organoid
treatment
differentiation
stemness
TFF1
TFF3
MUC2
ASCL2
AXIN1
AXIN2
CD44
CTNNB1
LGR5
log2FC
BRAFi
MEKi
mTORi
PI3Ki
TAKi
TBKi
*p-value < 0.01
F
CRC02
relative mRNA expression
G
CRC26
DMSO

Figure 5

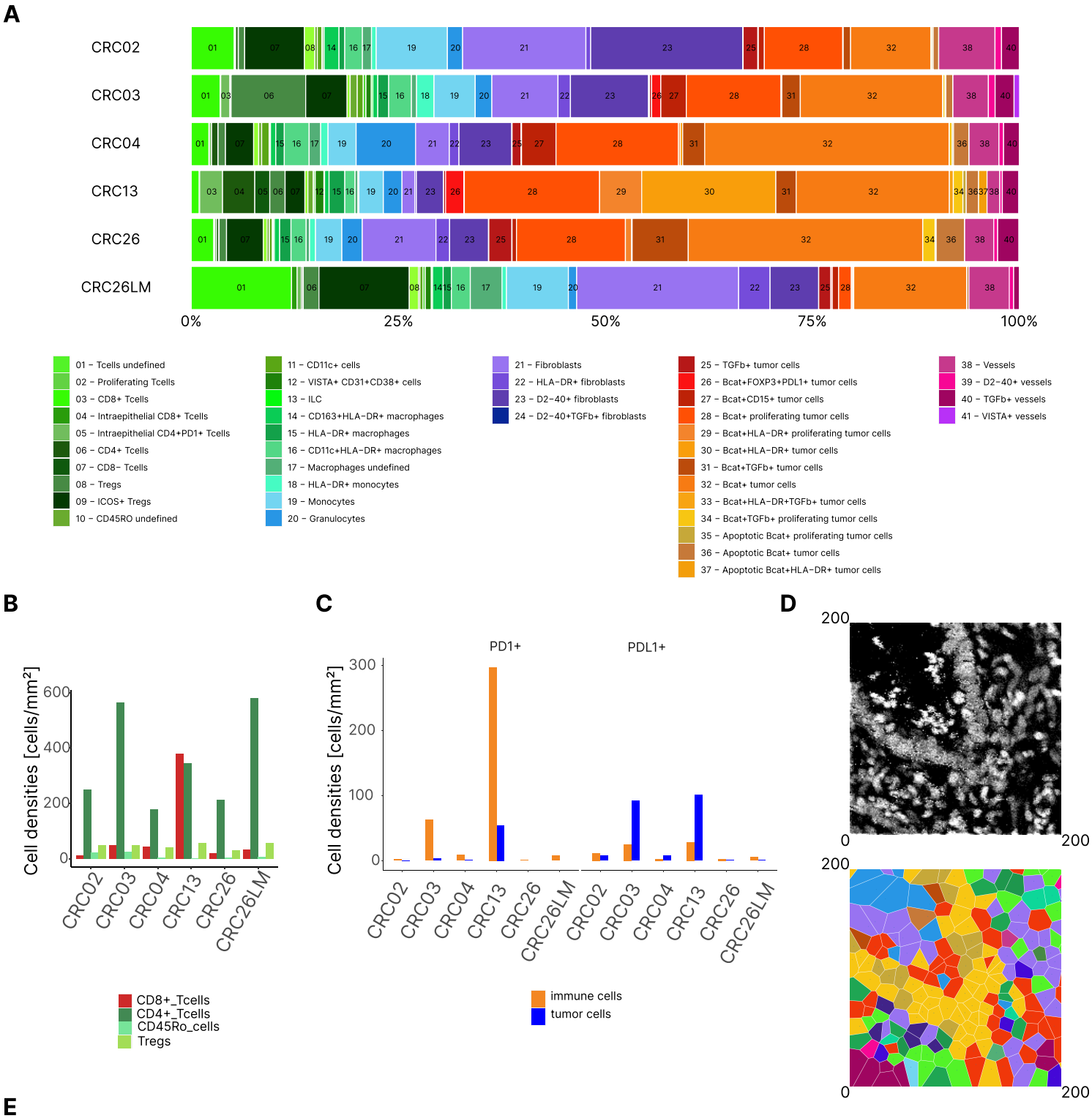
A
CRC02
CRC03
CRC04
CRC13
CRC26
CRC26LM
0%
25%
50%
75%
100%
01 – Tcells undefined
02 – Proliferating Tcells
03 – CD8+ Tcells
04 – Intraepithelial CD8+ Tcells
05 – Intraepithelial CD4+PD1+ Tcells
06 – CD4+ Tcells
07 – CD8− Tcells
08 – Tregs
09 – ICOS+ Tregs
10 – CD45RO undefined
11 – CD11c+ cells
12 – VISTA+ CD31+CD38+ cells
13 – ILC
14 – CD163+HLA−DR+ macrophages
15 – HLA−DR+ macrophages
16 – CD11c+HLA−DR+ macrophages
17 – Macrophages undefined
18 – HLA−DR+ monocytes
19 – Monocytes
20 – Granulocytes
21 – Fibroblasts
22 – HLA−DR+ fibroblasts
23 – D2−40+ fibroblasts
24 – D2−40+TGFb+ fibroblasts
25 – TGFb+ tumor cells
26 – Bcat+FOXP3+PDL1+ tumor cells
27 – Bcat+CD15+ tumor cells
28 – Bcat+ proliferating tumor cells
29 – Bcat+HLA−DR+ proliferating tumor cells
30 – Bcat+HLA−DR+ tumor cells
31 – Bcat+TGFb+ tumor cells
32 – Bcat+ tumor cells
33 – Bcat+HLA−DR+TGFb+ tumor cells
34 – Bcat+TGFb+ proliferating tumor cells
35 – Apoptotic Bcat+ proliferating tumor cells
36 – Apoptotic Bcat+ tumor cells
37 – Apoptotic Bcat+HLA−DR+ tumor cells
38 – Vessels
39 – D2−40+ vessels
40 – TGFb+ vessels
41 – VISTA+ vessels
B
Cell densities [cells/mm²]
CRC02
CRC03
CRC04
CRC13
CRC26
CRC26LM
CD8+_Tcells
CD4+_Tcells
CD45Ro_cells
Tregs
C
PD1+
PDL1+
Cell densities [cells/mm²]
immune cells
tumor cells
D
E
460
0
650

Figure 6

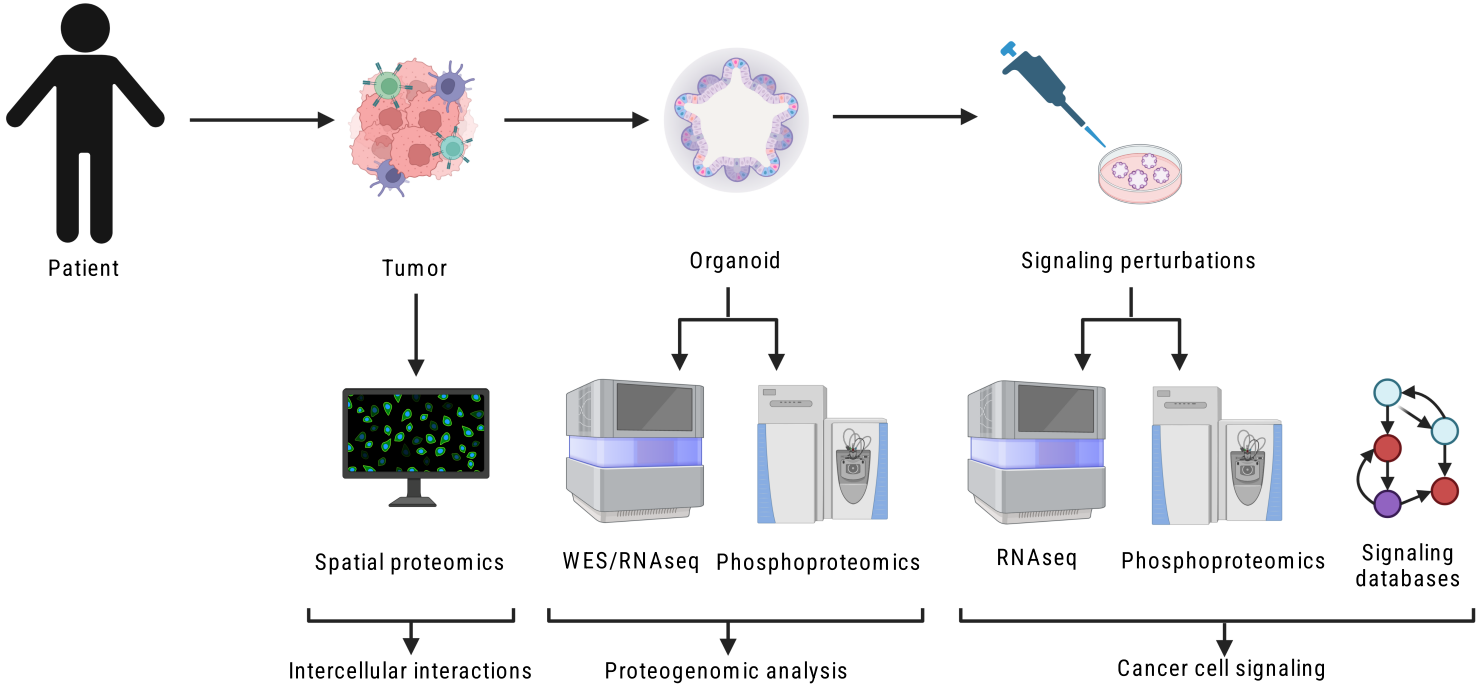
Patient
Tumor
Organoid
Signaling perturbations
Spatial proteomics
WES/RNAseq
Phosphoproteomics
RNAseq
Phosphoproteomics
Signaling databases
Intercellular interactions
Proteogenomic analysis
Cancer cell signaling

Figure 1

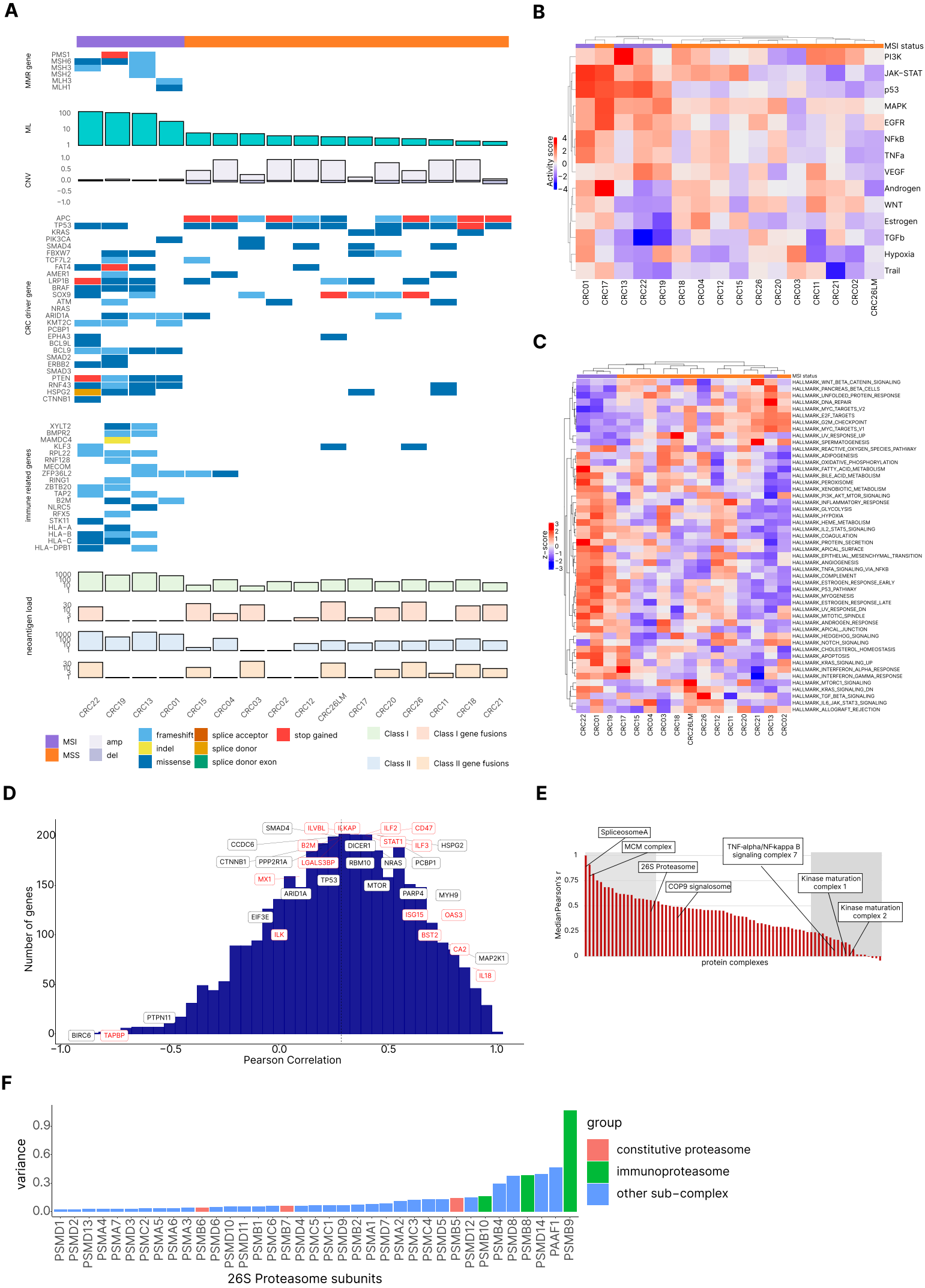
A
MMR gene
PMS1
MSH6
MSH3
MSH2
MLH3
MLH1
ML
CNV
CRC driver gene
APC
TP53
KRAS
PIK3CA
SMAD4
FBXW7
TCF7L2
FAT4
AMER1
LRP1B
BRAF
SOX9
ATM
NRAS
ARID1A
KMT2C
PCBP1
EPHA3
BCL9L
BCL9
SMAD2
ERBB2
SMAD3
PTEN
RNF43
HSPG2
CTNNB1
immune related genes
XYLT2
BMPR2
MAMDC4
KLF3
RPL22
RNF128
MECOM
ZFP36L2
RING1
ZBTB20
TAP2
B2M
NLRC5
RFX5
STK11
HLA-A
HLA-B
HLA-C
HLA-DPB1
neoantigen load
CRC22
CRC19
CRC13
CRC01
CRC15
CRC04
CRC03
CRC02
CRC12
CRC26LM
CRC17
CRC20
CRC26
CRC11
CRC18
CRC21
MSI
MSS
amp
del
frameshift
indel
missense
splice acceptor
splice donor
splice donor exon
stop gained
Class I
Class II
Class I gene fusions
Class II gene fusions
B
MSI status
PI3K
JAK-STAT
p53
MAPK
EGFR
NFkB
TNFa
VEGF
Androgen
WNT
Estrogen
TGFb
Hypoxia
Trail
Activity score
CRC01
CRC17
CRC13
CRC22
CRC19
CRC18
CRC04
CRC12
CRC15
CRC26
CRC20
CRC03
CRC11
CRC21
CRC02
CRC26LM
C
MSI status
HALLMARK_WNT_BETA_CATENIN_SIGNALING
HALLMARK_PANCREAS_BETA_CELLS
HALLMARK_UNFOLDED_PROTEIN_RESPONSE
HALLMARK_DNA_REPAIR
HALLMARK_MYC_TARGETS_V2
HALLMARK_E2F_TARGETS
HALLMARK_G2M_CHECKPOINT
HALLMARK_MYC_TARGETS_V1
HALLMARK_UV_RESPONSE_UP
HALLMARK_SPERMATOGENESIS
HALLMARK_REACTIVE_OXYGEN_SPECIES_PATHWAY
HALLMARK_ADIPOGENESIS
HALLMARK_OXIDATIVE_PHOSPHORYLATION
HALLMARK_FATTY_ACID_METABOLISM
HALLMARK_BILE_ACID_METABOLISM
HALLMARK_PEROXISOME
HALLMARK_XENOBIOTIC_METABOLISM
HALLMARK_PI3K_AKT_MTOR_SIGNALING
HALLMARK_INFLAMMATORY_RESPONSE
HALLMARK_GLYCOLYSIS
HALLMARK_HYPOXIA
HALLMARK_HEME_METABOLISM
HALLMARK_IL2_STAT5_SIGNALING
HALLMARK_COAGULATION
HALLMARK_PROTEIN_SECRETION
HALLMARK_APICAL_SURFACE
HALLMARK_EPITHELIAL_MESENCHYMAL_TRANSITION
HALLMARK_ANGIOGENESIS
HALLMARK_TNFA_SIGNALING_VIA_NFKB
HALLMARK_COMPLEMENT
HALLMARK_ESTROGEN_RESPONSE_EARLY
HALLMARK_P53_PATHWAY
HALLMARK_MYOGENESIS
HALLMARK_ESTROGEN_RESPONSE_LATE
HALLMARK_UV_RESPONSE_DN
HALLMARK_MITOTIC_SPINDLE
HALLMARK_ANDROGEN_RESPONSE
HALLMARK_APICAL_JUNCTION
HALLMARK_HEDGEHOG_SIGNALING
HALLMARK_NOTCH_SIGNALING
HALLMARK_CHOLESTEROL_HOMEOSTASIS
HALLMARK_APOPTOSIS
HALLMARK_KRAS_SIGNALING_UP
HALLMARK_INTERFERON_ALPHA_RESPONSE
HALLMARK_INTERFERON_GAMMA_RESPONSE
HALLMARK_MTORC1_SIGNALING
HALLMARK_KRAS_SIGNALING_DN
HALLMARK_TGF_BETA_SIGNALING
HALLMARK_IL6_JAK_STAT3_SIGNALING
HALLMARK_ALLOGRAFT_REJECTION
z-score
CRC22
CRC01
CRC19
CRC17
CRC15
CRC04
CRC03
CRC18
CRC26LM
CRC26
CRC12
CRC11
CRC20
CRC21
CRC13
CRC02
D
Number of genes
Pearson Correlation
SMAD4
ILVBL
ILKAP
ILF2
CD47
CCDC6
B2M
DICER1
STAT1
ILF3
HSPG2
CTNNB1
PPP2R1A
LGALS3BP
RBM10
NRAS
PCBP1
MX1
TP53
MTOR
ARID1A
PARP4
MYH9
EIF3E
ISG15
OAS3
ILK
BST2
CA2
MAP2K1
IL18
PTPN11
BIRC6
TAPBP
E
Spliceosome A
MCM complex
26S Proteasome
COP9 signalosome
TNF-alpha/NF-kappa B signaling complex 7
Kinase maturation complex 1
Kinase maturation complex 2
Median Pearson's r
protein complexes
F
variance
26S Proteasome subunits
group
constitutive proteasome
immunoproteasome
other sub-complex
PSMD1
PSMD2
PSMD13
PSMA4
PSMA7
PSMD3
PSMC2
PSMA5
PSMA6
PSMA3
PSMB6
PSMD6
PSMD10
PSMD11
PSMB1
PSMC6
PSMB7
PSMD4
PSMC5
PSMC1
PSMD9
PSMB2
PSMA1
PSMD7
PSMA2
PSMC3
PSMC4
PSMD5
PSMB5
PSMD12
PSMB10
PSMB4
PSMD8
PSMB8
PSMD14
PAAF1
PSMB9

Figure 2